

This Page Is Inserted by IFW Operations  
and is not a part of the Official Record

## **BEST AVAILABLE IMAGES**

Defective images within this document are accurate representations of the original documents submitted by the applicant.

Defects in the images may include (but are not limited to):

- BLACK BORDERS
- TEXT CUT OFF AT TOP, BOTTOM OR SIDES
- FADED TEXT
- ILLEGIBLE TEXT
- SKEWED/SLANTED IMAGES
- COLORED PHOTOS
- BLACK OR VERY BLACK AND WHITE DARK PHOTOS
- GRAY SCALE DOCUMENTS

**IMAGES ARE BEST AVAILABLE COPY.**

**As rescanning documents *will not* correct images,  
please do not report the images to the  
Image Problem Mailbox.**

# UV RESONANCE RAMAN STUDIES OF MOLECULAR STRUCTURE AND DYNAMICS: Applications in Physical and Biophysical Chemistry

*Sanford A. Asher*

Department of Chemistry, University of Pittsburgh, Pittsburgh,  
Pennsylvania 15260

## INTRODUCTION

A fundamental understanding of molecular structure and dynamics requires a close coupling between theory and experiment. One ultimate objective is to utilize the understanding of molecular structure and dynamics to predict both molecular properties such as chemical reactivity and bulk properties such as phase behavior and material strengths. Often the major driving force for progress in science is the development of new experimental techniques capable of incisive glimpses into simple phenomena in complex systems. This is especially important for studies of large polyatomic molecules, and is crucial for the macromolecules studied in biology and biochemistry that control life processes.

This review outlines the recent progress in the development of UV resonance Raman spectroscopy (UVR) as a new technique for the study of molecular structure and dynamics for both small molecules and larger molecules such as polypeptides and proteins. This recent work follows the pioneering UV Raman nucleic acid studies in 1975, which used frequency doubled Ar laser excitation at 257 nm (1-4), and Ziegler & Albrecht's pioneering nitrogen-dye laser preresonance Raman benzene derivative studies, which set the stage for true resonances. Raman investigations of benzene derivatives and other aromatics (5-8). This work was followed by

Ziegler & Hudson's UV resonance Raman benzene-derivative studies excited at 212.8 nm using a quintupled Yag laser (9, 10). Intense activity began in 1983 as tunable Nd-Yag based excitation sources became available (*wide infra*).

Raman spectroscopy monitors the coupling between electromagnetic radiation and the component of the molecular polarizability that is modulated by molecular vibrations (11). Thus, the Raman effect derives directly from dynamical coupling between electronic and vibrational motion. Excitation in resonance within a particular electronic transition results in Raman scattering that is dominated by the dynamical vibrational-electronic coupling present within the resonant rovibronic excited state. UV excitation (below 300 nm) occurs in the spectral region that is dominated by the electronic transitions of frontier orbitals of both small molecules and of small chromophoric segments of large macromolecular systems. Thus, UV Raman scattering can monitor the ro-vibronic-electronic dynamics of the excited states of small molecules such as ammonia, methyl iodide, and benzene. These small molecules are the modern candidates for theoretical electronic studies that attempt to calculate excited state geometries, dynamics, and potential surfaces. These theoretical studies have over the last 30 years remained at the frontier of physical chemistry as the sophistication of the calculations have increased and as the size of the molecules examined have increased. UV resonance Raman spectroscopy offers a major new experimental probe of the dynamics within the excited states of interest.

The selective examination of isolated segments of macromolecules is essential for progress in biochemistry and polymer science. UV resonance Raman spectroscopy can be used to excite particular chromophoric segments of proteins (12, 13). To the extent that the protein structure, conformation, and enzymatic reactivity are direct consequences of specific intermolecular interactions between amino acid residues, it may be possible to excite selectively those specific amino acid residues directly involved in the reaction coordinate in order to obtain information to help elucidate the enzymatic mechanism. As discussed in this review, rapid progress is being made in biophysical applications of UVRR. Many of these studies probe aromatic amino acids in proteins and take advantage of the numerous previous studies of simpler aromatic molecules. In addition, other recent UVRR biophysical studies take advantage of UV photochemistry to examine transient photochemically generated excited states. These studies probe the dynamics of return of these excited state species to the ground state.

In this review I examine UVRR instrumentation, the basic resonance Raman scattering phenomenology, and discuss studies that probe dynamics

in the excited states of small molecules such as ammonia, ethylene, benzene and N-methyl acetamide. I also review some recent biophysical applications, and discuss two new emerging techniques, Saturation Raman Spectroscopy and Hyper-Raman Spectroscopy, which will have significant impact in the future.

## INSTRUMENTATION

### *Excitation Source*

The recent progress in UV Raman spectroscopy has been made possible by the development of UV laser excitation sources. The ideal excitation source for most UV Raman measurements would be a CW laser source that is conveniently tunable over the spectral region between 150 nm and 800 nm. In contrast, the conventional excitation source until recently was a high power, low duty cycle Nd-Yag based laser system. Figure 1, which shows a block diagram of our Raman spectrometer (14), indicates that we utilize a 20 Hz, 6 nsec Yag laser, which delivers ca 250 mJ per pulse at 1064  $\mu$ m. By using efficient harmonic generation crystals such as KDP, the Yag fundamental is frequency doubled or tripled to 532 or 355 nm in order to excite a dye laser. The dye laser output is frequency doubled down to ca 260 nm. Light between 217 and 260 nm is obtained by mixing the 1064 nm Yag fundamental with the doubled dye output. Excitation below 217 nm is obtained by anti-Stokes Raman shifting the quadrupled Yag excitation of 266 nm. In this way, light between 190 to 800 nm is generated. The pulse energy (average power) will vary from a minimum of less than 0.05 mJ (1 mW average power) below 217 nm to 1.0 mJ (20 mW) between 217-260 nm and to 10 mJ (200 mW) above 260 nm. In all cases the nonlinear optical efficiencies are high due to the short temporal pulse widths and the fact that high efficiency nonlinear crystals are used. Unfortunately the short pulse widths result in extraordinarily high peak power or energy fluxes if the excitation source is tightly focused in the sample in order to optimize collection efficiency of the scattered light. For example, 6 nsec, 1 mJ pulses focused to a 0.1 mm diameter in the sample have peak powers and peak energy fluxes of ca 2 GigaWatts  $\text{cm}^{-2}$  and 10 J  $\text{cm}^{-2}$ . This commercially available laser system is easily and continuously tunable over the 217-800 nm spectral region. The major inconvenience derives from the necessity for changing dyes if excitation is to span a UV spectral region larger than ca 10-20 nm.

Other laboratories have used a single high power Yag laser to generate numerous discreet UV excitation lines between 320 and 184 nm (15, 16). These lines are generated by anti-Stokes Raman shifting the doubled, tripled, or quadrupled Yag beam in hydrogen gas. The high peak power

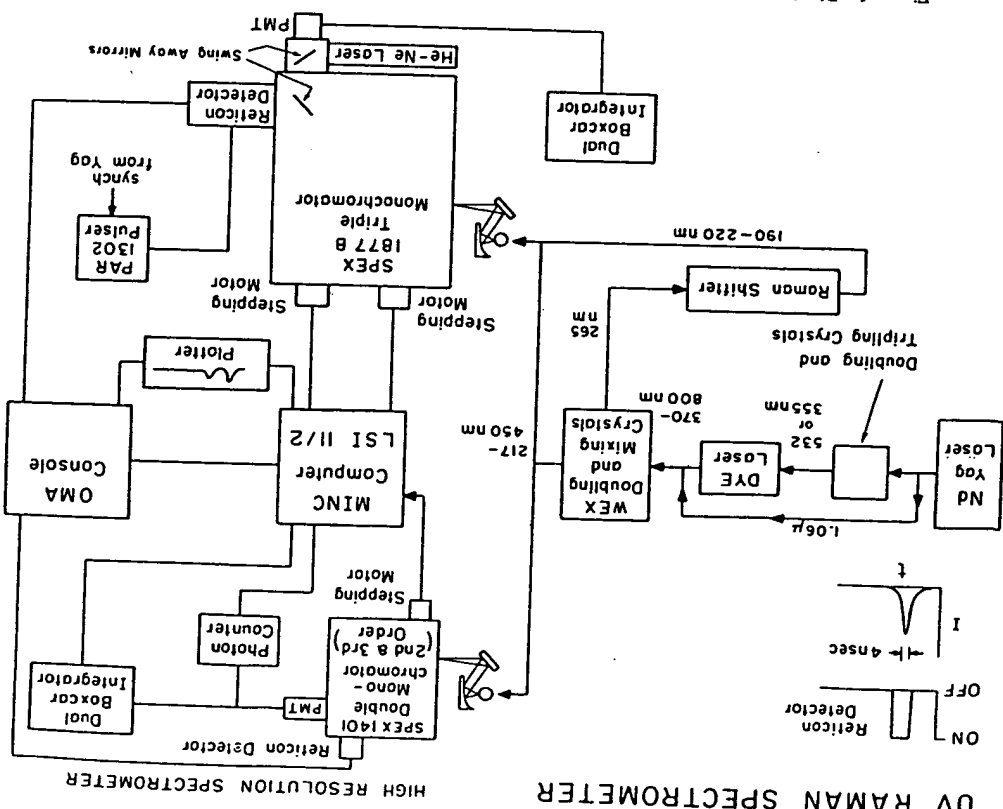
Yag beam, when focused into a tube of hydrogen gas pressurized between two and five atmospheres, will stimulate Raman scattering to generate a number of anti-Stokes wavelengths that are shifted by harmonics of  $4155\text{ cm}^{-1}$ , the hydrogen-stretching frequency. The efficiency of Raman shifting is very high for the high Yag peak powers and is often greater than 10% for the first anti-Stokes line. Ziegler (17) has developed a continuously tunable UV excitation source by anti-Stokes Raman shifting a Yag-pumped dye laser into the deep UV spectral region close to 200 nm.

The high pulse energies and the peak powers of the low duty cycle Yag excitation sources often induce optical phenomena that can interfere with the Raman spectral measurements (18, 19). Saturation of the Raman intensities can occur due to depletion of the ground state species during the laser excitation pulse. This saturation makes measurements of Raman cross-sections and relative intensities difficult and presents insidious potential artifacts for protein studies. For example, different protein aromatic amino acids show different ground state recovery rates and, thus, show different amounts of saturation; the protein aromatic amino acid relative intensities become power dependent. Interferences can also occur as a result of Raman scattering from high concentrations of photochemical intermediates. In addition, other photochemical processes can occur, such as two-photon ionization processes, to cause sample decomposition.

Stimulated Raman scattering can also complicate the Raman studies. Recently we demonstrated the utility of a high repetition rate excimer laser for decreasing the pulse energies to permit excitation at higher average powers (19). This lower pulse energy excitation helps to avoid saturation and other photochemical artifacts. The recent discovery that  $\beta$ -barium borate crystals can be used to frequency-double light efficiently into the 200–300 nm spectral region should make high repetition rate (greater than 500 Hz) excimer-pumped dye lasers the standard UV excitation source (20, 21); 500 Hz, 16 nsec pulse duration excimer laser sources are commercially available. The high efficiency (greater than 25% at 240 nm) of these  $\beta$ -barium borate frequency doubling crystals permits dramatic reductions in the required dye laser output, with concomitant reductions in the required excimer pump power. The delayed acceptance of excimer based UV Raman excitation sources derived mainly from the extraordinarily high projected costs for dye replacement (22). The poor "doubling efficiencies below 260 nm of the previously available frequency doubling crystals necessitated extraordinarily high excimer pump powers to generate sufficient dye laser output to achieve modest levels (ca 20 mW average) of UV power below 260 nm. The development of the highly efficient  $\beta$ -barium borate crystals should dramatically decrease the dye replacement costs.

Other groups have attempted to use an injection-locked excimer laser

Figure 1. Block diagram of a tunable UV resonance Raman spectrometer. After Ref. (14).



UV RAMAN SPECTROMETER

as an excitation source. The narrow excimer excitation was to be used both directly and Raman shifted to obtain other wavelengths. Reliable and stable injection locking that prevents excitation wavelength hopping over the excimer gain curve has not as yet become routine and represents the main impediment for this laser excitation source.

#### *Sample Handling and Collection Optics*

Standard optics are used to focus the laser excitation into the sample and to collect and focus the scattered light into the spectrometer. We utilized a  $\text{MgF}_2$ -coated aluminized ellipsoidal mirror as the achromatic collection optic for our spectrometer to avoid the chromatic aberrations that lead to artifacts in intensity and excitation profile measurements. However,  $\text{MgF}_2$  or quartz lenses are more convenient and may be more efficient if scattering occurs from nonpoint-like illuminated sample volumes; the ellipsoidal mirror is efficient for light collection from point sources.

The sample handling accessories are simple for gases, and typically involve flowing the gas through a nozzle. The gas stream is intersected by the laser excitation beam prior to the evacuation to a fume hood. For combustible mixtures, an annulus of flowing nitrogen surrounds the sample gas flow. Simple quartz cells filled with static sample gases have also been used when photochemistry did not interfere with the spectral measurements.

Liquid sample handling systems are more complex and are designed to replenish the sample volume between laser pulses. Sample solutions are circulated through thin quartz capillaries by using a peristaltic pump. It is important to avoid interference from plasticizers used in the rubber tubing, which can leach into the sample solutions. Other liquid sample handling systems attempt to avoid the nonlinear optical phenomena that often occur at surfaces to degrade the sample; opaque material deposits on the capillary walls to prevent transmission of the excitation beam into the sample. A thin ( $200\ \mu\text{m}$ ) free lamellar jet of liquid can be prepared by recirculating sample solutions through a dye laser jet nozzle by using a high pressure pump (14). An exterior cylindrical quartz tube can be used to isolate the liquid stream in order to establish vapor equilibrium to avoid solvent evaporation. The jet stream is rectangular and is ca.  $0.2\ \mu\text{m}$  wide and  $3\ \mu\text{m}$  high. The sides of the stream are optically flat and parallel. Excitation can occur either at an angle to the flat surface, or  $90^\circ$  scattering can be accomplished by focusing into the narrow edge. The rapid flow and the unconstrained walls make this sampling system useful for high repetition laser excitation. Further, the thinness of the jet prevents significant self-absorption.

Another approach utilizes gentle flow through a capillary that has a

hole drilled in the wall (23). For gentle lamellar flow with minimal back pressure, surface tension constrains the liquid, and a free surface can be excited by backscattering from the hole in the side. A free flowing liquid surface has also been prepared by flowing sample solutions down a pair of separated wires (24) or down a teflon tube that was cut and shaped such that the surface tension of the liquid formed a flat surface (23).

Solid samples have not generally been studied in the UV. The potential difficulties for studying them with pulsed laser excitation are obvious; the illuminated solid volume element must be replaced between laser pulses and the sample must have sufficient thermal conductivity (via linear or nonlinear processes) to remove the energy deposited during each pulse without significant thermal decomposition during the laser pulse.

#### *Spectrometer and Detection System*

The spectrometer and detection systems typically used fall into two categories: Either a complex spectrometer is used that contains a predispersing system to reject the Rayleigh scattering, followed by a spectrograph and multichannel detector, or a single high dispersion, long pathlength monochromator is used combined with a solar blind photomultiplier and boxcar detection. The single monochromator/solar blind photomultiplier detection system has a high dynamic range and high throughput efficiency (as high as 60–70%).

The photomultiplier detector is shot-noise limited. The use of a high dispersion grating and adjustable slits permits high resolution gas phase studies (to the bandwidth of the laser excitation, typically  $1\ \text{cm}^{-1}$ ). The instrumentation is relatively inexpensive and rugged. Unfortunately, stray light can interfere in low frequency Raman measurements due to the inability of the single grating to reject all of the Rayleigh scattered light. Another disadvantage of the scanning systems is that only a small fraction of the spectrum is examined at any time; the signal-to-noise limitations are not generally shot-noise limited. Most of the noise in pulsed laser measurements derive from pulse-to-pulse fluctuations in Raman scattering due to fluctuations in energy, and spatial and temporal beam shapes. A portion of these fluctuations can be normalized out by using dual channel boxcar detection, where the detected Raman intensity for each pulse is normalized to the incident energy.

The multichannel Raman spectrometer shown in Figure 1 utilizes a Spex Triplemate spectrometer and an intensified Reticon Array (EG&G OMA II Model 1420). The predispersing stage uses a subtractive double spectrometer to remove the Rayleigh scattering and transfers the Raman scattered light to a  $0.64\ \text{nm}$  spectograph, which disperses and images the light onto the detector. Although the transfer efficiency of this spec-

graph has been measured to be low (ca. 3%), the multichannel advantage more than compensates for this throughput loss. For the Reticon detector, a large fraction of the Raman spectrum is simultaneously accumulated (ca. 1500 cm<sup>-1</sup>), and this automatically normalizes out pulse-to-pulse fluctuations. Unfortunately, the ultimate low signal limit for the intensified Reticon detector derives from background electronic noise. This means that signal strengths below the detector noise levels cannot be observed; increasing the integration time proportionately increases both the signal and the noise. New multichannel detectors, such as charge coupled devices (CCDs), are emerging that have high sensitivities and lower noise levels (26, 27). Multichannel spectrometers such as shown in Figure 1 show high sensitivity and reasonably low stray light above 400 cm<sup>-1</sup>, but have relatively modest resolution in the UV; the typically useful resolution is ca. 5 cm<sup>-1</sup> at 240 nm, which is determined by the spectrograph grating and the effective Reticon element pixel width. However, this resolution is adequate for most condensed phase studies. The multichannel spectrophotograph is ideal for monitoring small frequency shifts; since no mechanical changes occur between separate scans. Obviously, the ideal spectrometer would be a single high dispersion spectrometer designed to minimize stray light equipped with a multichannel detector.

## RAMAN PHENOMENOLOGY

The Raman effect derives from the inelastic scattering of electromagnetic radiation by matter. For the purposes of this review the energy exchange is mainly limited to vibrational energy quanta. Figure 2 shows an energy level diagram for production of Stokes Raman scattering, where a molecule in its vibronic ground state is excited by light of frequency  $\nu_0$ . Raman shifted light is Stokes scattered at frequencies  $\nu_0 - \nu_a$  and  $\nu_0 - \nu_b$ , where  $\nu_a$  and  $\nu_b$  are vibrational mode frequencies. Obviously the molecule is pro-

moted to higher vibrational quantum levels of the ground electronic state during this process. Molecular spectroscopic information is conveyed by the vibrational frequency shift, by the efficiency (intensity) of the Raman scattering process, and by the polarization of the Raman scattered light relative to the incident scattering.

The vibrational frequency shifts derive from the nuclear vibrational dynamics that occur within the ground state of the molecule. Every molecule (nonlinear) has 3N-6 normal modes of vibration, each of which has a characteristic frequency of oscillation that depends upon interatomic force constants, atomic masses, and the couplings with the motion of both adjacent and distant atoms. The ability to calculate these normal mode frequencies and motions represents one of the great successes of physical chemistry. The Raman frequencies directly report upon the ground state molecular structure and intermolecular interactions, such as the presence of hydrogen bonding, for example. The Raman bandwidths in the condensed phase depend upon dynamical processes that control lifetimes of the ground state vibronic levels (homogeneous linewidth) and/or the distribution of molecular environments (inhomogeneous linewidth) (28, 29a,b).

The Raman band intensities at a particular excitation frequency depend upon the degree to which a particular vibration modulates the molecular polarizability. For excitation at frequency  $\nu_0$ , the Raman intensity,  $I_{nm}$ , observed over a unit solid angle for a Raman transition between vibronic levels  $n$  and  $m$  in the electronic ground state manifold is (30-34)

$$I_{nm} = \sigma_{nm}^R N I_0 W(\Omega)$$

where  $\sigma_{nm}^R$  (cm<sup>2</sup> · mol<sup>-1</sup> · str<sup>-1</sup>) is the total differential Raman cross-section for a single gas phase molecule integrated over the Raman peak bandwidth.  $I_0$  is the incident excitation intensity (photons · cm<sup>-2</sup> sec<sup>-1</sup>) into a particular sample volume element of area  $dA$  and length  $dl$ ,  $N$  is the number of molecules within that volume element, and  $W(\Omega)$  is a parameter that details the optical geometry and includes factors such as the collected solid angle. For a single orientationally averaged molecule in vacuum, the differential Raman scattering cross-section may be written

$$\sigma_{nm}^R = 4\pi^2 \left( \frac{e^2}{\hbar c} \right) \nu_0 (\nu_0 - \nu_{nm})^3 g f(T) \left| \sum_{\rho\sigma} \overline{e_{\rho\sigma}^* e_{\rho\sigma}} \right|^2$$

where  $e^2/\hbar c$  is the fine structure constant, and  $\nu_0$  and  $\nu_{nm}$  are the frequencies (cm<sup>-1</sup>) of the excitation source and the Raman active vibration, respectively.  $g$  is a factor specifying the degree of degeneracy of the vibration, while  $f(T)$  is the Boltzmann weighting factor specifying the thermal occu-

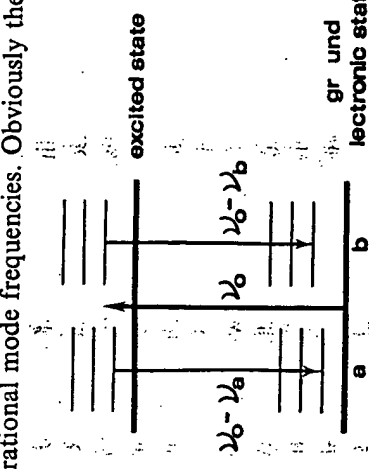


Figure 2 Illustration of Raman vibrational transitions.

pacity of the initial state,  $m$ .  $\alpha_{\rho\sigma}$  is the  $\rho\sigma$ th element of the polarizability tensor where  $\rho$  and  $\sigma$  are molecular fixed coordinates,  $s$  and  $0$  are lab fixed coordinates, and  $e_{\tau 0}$  and  $e_{\nu 0}$  represent unit vectors that point in the polarization directions of the excitation and scattered light, respectively. The expression

$$\left| \sum_{\rho\sigma} e_{\nu\rho}^* \alpha_{\rho\sigma} e_{\sigma 0} \right|^2$$

indicates that the value of  $\alpha_{\rho\sigma}$  is averaged over all possible molecular orientations, given particular values of  $e_{\nu 0}$  and  $e_{\tau 0}$ . Typically, the differential Raman cross-section,  $\sigma_m^R$ , is measured in units of Barns str<sup>-1</sup> (1 Barn =  $10^{-24}$  cm<sup>2</sup> · mol<sup>-1</sup>), and Raman cross-sections of species such as hexane, benzene, and acetone have cross-sections of ca  $1.0 \times 10^{-6}$  Barns str<sup>-1</sup> with visible wavelength excitation (31, 32). The strongest resonance Raman cross-sections observed are greater than 60 Barns str<sup>-1</sup>.

The total differential Raman cross-section includes light polarized both parallel and perpendicular to the incident polarization (Figure 3). For the typical 90° scattering geometry where the molecule occurs randomly oriented in the gas, solution, or solid phase, and where we collect both parallel and perpendicular scattering components, it is convenient to write the Raman differential cross-section in terms of the Raman polarizability tensor invariants  $\Sigma^0$ ,  $\Sigma^1$ ,  $\Sigma^2$  (34).

$$5. \quad \Sigma^0 = \frac{1}{3} |\alpha_{xx} + \alpha_{yy} + \alpha_{zz}|^2$$

$$\Sigma^1 = \frac{1}{2} \{ |\alpha_{xy} - \alpha_{yx}|^2 + |\alpha_{xz} - \alpha_{zx}|^2 + |\alpha_{yz} - \alpha_{zy}|^2 \}$$

$$\Sigma^2 = \frac{1}{2} \{ |\alpha_{xy} + \alpha_{yx}|^2 + |\alpha_{xz} + \alpha_{zx}|^2 + |\alpha_{yz} + \alpha_{zy}|^2 \}$$

$$+ \frac{1}{3} \{ |\alpha_{xx} - \alpha_{yy}|^2 + |\alpha_{xx} - \alpha_{zz}|^2 + |\alpha_{yy} - \alpha_{zz}|^2 \}$$

$\Sigma^0$ ,  $\Sigma^1$ , and  $\Sigma^2$  are known as the isotropic (trace), the antisymmetric anisotropic, and the symmetric anisotropic Raman invariants, respectively.

For nonresonance Raman scattering,  $\Sigma^1$ , the antisymmetric tensor component is zero, since the tensor is symmetric. Although for resonance Raman scattering  $\Sigma^1$  may become large for particular vibrational symmetries in particular point groups, it vanishes for the examples discussed here.

The Raman depolarization ratio is the relative intensity ratio of Raman scattering observed perpendicular,  $I_{\perp}$ , and parallel,  $I_{\parallel}$ , to the incident polarization. The depolarization ratio can be calculated directly from the relative values of the Raman invariants

$$6. \quad \rho = \frac{(I_{\perp})}{(I_{\parallel})} = \frac{5\Sigma^1 + 3\Sigma^2}{10\Sigma^0 + 4\Sigma^2}.$$

If  $\Sigma^1$  is zero,  $\rho$  will vary between a value of 0.00 and 0.75, since the invariants are positive definite quantities. If only one tensor element

$$\sigma_{nm} = \sigma_{nm}^R(90^\circ, \parallel + \perp) = 4\pi^2 \left( \frac{e^2}{\hbar c} \right)^2 v_0 (\nu_0 - \nu_{nm})^3 g f(T) L(\nu_0)$$

$$\times (10\Sigma^0 + 5\Sigma^1 + 7\Sigma^2)$$

3. The expression where  $L(\nu_0)$  details the increased local electromagnetic field strength within the sample medium over that in vacuum. The local field correction is suggested to be modeled accurately as (31, 32, 35)

$$L(\nu_0) = (n_s/n_0)(n_s^2 + 2)^2(n_0^2 + 2)^2/81$$

where  $n_s$  and  $n_0$  are the refractive indices for light at the incident and Raman scattered frequency, respectively.

The Raman tensor invariants are those linear combinations of Raman tensor elements which turn out to be independent of the relative orientation between the molecular and laboratory frames.

$$7. \quad \Sigma^0 = \frac{1}{3} |\alpha_{xx} + \alpha_{yy} + \alpha_{zz}|^2$$

$$\Sigma^1 = \frac{1}{2} \{ |\alpha_{xy} - \alpha_{yx}|^2 + |\alpha_{xz} - \alpha_{zx}|^2 + |\alpha_{yz} - \alpha_{zy}|^2 \}$$

$$\Sigma^2 = \frac{1}{2} \{ |\alpha_{xy} + \alpha_{yx}|^2 + |\alpha_{xz} + \alpha_{zx}|^2 + |\alpha_{yz} + \alpha_{zy}|^2 \}$$

$$+ \frac{1}{3} \{ |\alpha_{xx} - \alpha_{yy}|^2 + |\alpha_{xx} - \alpha_{zz}|^2 + |\alpha_{yy} - \alpha_{zz}|^2 \}$$

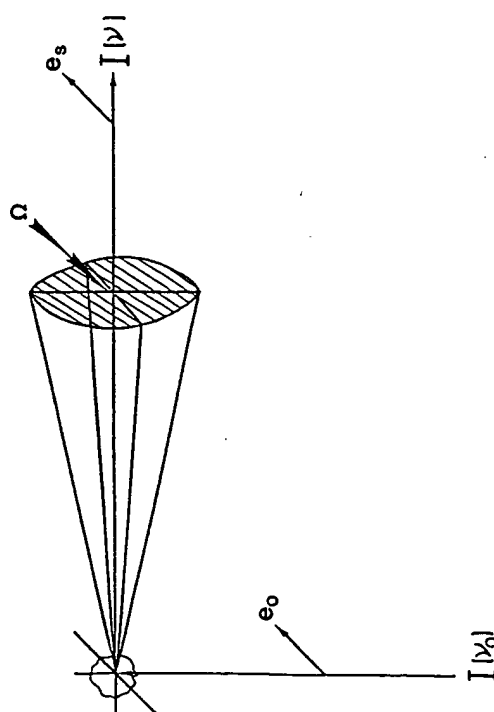


Figure 3 Raman 90° scattering geometry.

say  $\alpha_{xx}$ , is greater than zero,  $\rho = 0.33$ . For  $\alpha_{xx} = \alpha_{yy}$  and  $\alpha_{zz} = \alpha_{xy} = \alpha_{xz} = \alpha_{yz} = 0$ ,  $\rho = 0.125$ . For  $\alpha_{xx} = \alpha_{yy} = \alpha_{zz}$ , with all of the off-diagonal elements equal to zero,  $\rho = 0.00$ . Finally if  $\alpha_{xx} = \sigma_{xx} = \alpha_{zz} = 0$  and off-diagonal elements are different from zero, then  $\rho = 0.75$ . Obviously, the depolarization ratio is very sensitive to the relative values of the Raman polarizability tensor elements and can be used to examine both electronic and vibrational dynamics for a Raman scattering process where the scattering time is essentially instantaneous relative to molecular rotation periods. If the scattering time becomes long compared to the rotational period,  $\rho$  will approach a value of 1.0 since the molecule rotates prior to emission and the polarization becomes isotropic.

We must specify  $\alpha_{\rho\rho}$  in terms of the molecular electronic and vibrational states. For this review I mainly rely on the familiar sum over states given by the Kramer Heisenberg-Dirac (KHD) formalism. It should be noted, however, that significant advances have recently been made in applying the propagating wave packet formalism of Lee & Heller (36, 37) to relate observed Raman cross sections to excited state potential surfaces. In fact, the wave packet formalism derives directly from the KHD expression through an inverse Laplace transform. The time dependent formalism, however, has been extraordinarily useful in describing dissociative excited state surfaces for molecules like  $\text{CH}_3\text{J}$  where the observed Raman cross-sections for the molecular vibrational normal modes can be related to the dynamical dissociation coordinates (38-40). However, most of the recent UV Raman studies have utilized the KHD approach for physical insight. The KHD perturbation theory description of the Raman polarizability tensor elements is given by (30, 41)

$$\alpha_{\rho\rho} = \sum_{ev} \frac{\langle n|\mathbf{r}_\rho|ev\rangle\langle ev|\mathbf{r}_\sigma|m\rangle}{v_{ev}-v_0-i\Gamma_{ev}} + \frac{\langle n|\mathbf{r}_\sigma|ev\rangle\langle ev|\mathbf{r}_\rho|m\rangle}{v_{ev}+v_0-i\Gamma_{ev}} \quad 7.$$

where  $\mathbf{r}_\rho$  is an internal molecular coordinate specifying the position of each electron, where  $\mathbf{r}_\rho = \sum_e \mathbf{r}_{e\rho}$  and the summation occurs over all of the electrons.  $\alpha_{\rho\rho}$  has a contribution from all of the rovibronic molecular excited states as indicated by the summation over the excited states  $|ev\rangle$  in Eq. 7. The weighting of an individual  $|ev\rangle$  excited state contribution is determined by the values of the transition moment matrix elements in the numerator, and by the values of energy denominators. The energy denominators contain information on  $\Gamma_{ev}$ , the homogeneous linewidth for the transition between the ground state  $m$  and the excited state  $|ev\rangle$ , and the detuning of excitation from resonance,  $(v_{ev} - v_0)$ .

For normal Raman scattering, where excitation is far from resonance, all the denominator only weakly depends upon excitation frequency, and all

molecular rovibronic transitions contribute essentially in proportion to their transition moments. As resonance with an electronic transition is approached the first term of Eq. 7 begins to dominate, and the resonant excited state dominates the sum over states of the Raman polarizability expression. If we display the dependence of the transition moment matrix elements upon vibrational motion we can show that Eq. 7 will display three distinct scattering mechanisms (9, 42):

$$\alpha_{\rho\rho} = A + B + C:$$

$$A = \sum_{ev} \left[ \frac{\langle g|\mathbf{r}_\rho|e\rangle\langle e|\mathbf{r}_\sigma|g\rangle}{v_{ev}-v_0-i\Gamma_{ev}} \right] \langle f|v\rangle(v|i) \\ B = \sum_{ev} \left\{ \left[ \frac{\partial\langle g|\mathbf{r}_\rho|e\rangle}{\partial Q_a} \right]_0 \frac{\langle e|\mathbf{r}_\sigma|g\rangle}{v_{ev}-v_0-i\Gamma_{ev}} \right\} \langle f|Q_a|v\rangle(v|i) \\ + \left( \frac{\langle g|\mathbf{r}_\rho|e\rangle}{v_{ev}-v_0-i\Gamma_{ev}} \cdot \left[ \frac{\partial\langle e|\mathbf{r}_\sigma|g\rangle}{\partial Q_a} \right]_0 \right) \langle f|v\rangle(v|Q_a|i) \\ C = \sum_{ev} \sum_a \sum_b \left( \left[ \frac{\partial\langle g|\mathbf{r}_\rho|e\rangle}{\partial Q_a} \right]_0 \left[ \frac{\partial\langle e|\mathbf{r}_\sigma|g\rangle}{\partial Q_b} \right]_0 \right) \langle f|Q_a|v\rangle(v|Q_b|i). \quad 8.$$

The transition moment matrix elements have been factored into separate electronic and vibrational integrals. The transition moment integrals between the ground and excited electronic states are denoted by angular brackets. Curved brackets denote the integrals between vibrational levels, where  $|i\rangle$  labels the initial vibrational level of the normal mode  $a$  in the ground electronic state, and  $|v\rangle$  labels the final vibrational level of mode  $a$  in the excited electronic state.  $|f\rangle$  labels the final vibrational level of mode  $a$  in the ground electronic state ( $f = i+1$  for Stokes Raman scattering from mode  $a$ ).

A pictorial representation for these enhancement mechanisms is shown in Figure 4. Since the Raman cross-section is proportional to the modulus squared of the Raman polarizability, the  $A$ -term will dominate enhancement in strongly allowed transitions. The Raman cross-sections are proportional to the fourth power of the electronic transition moment to the resonant excited state. Thus, enhancement by a single electronic transition scales with the square of the molar absorptivity. The Franck-Condon overlap factors  $\langle f|v\rangle(v|i)$  will differ from zero only if the excited state equilibrium geometry is displaced along a symmetric normal mode coordinate relative to the ground state. This assumes identical *orthonormal* vibrational wavefunctions in the ground and excited states.  $A$ -term, Condon enhancement may also occur due to strong Franck-Condon overlaps

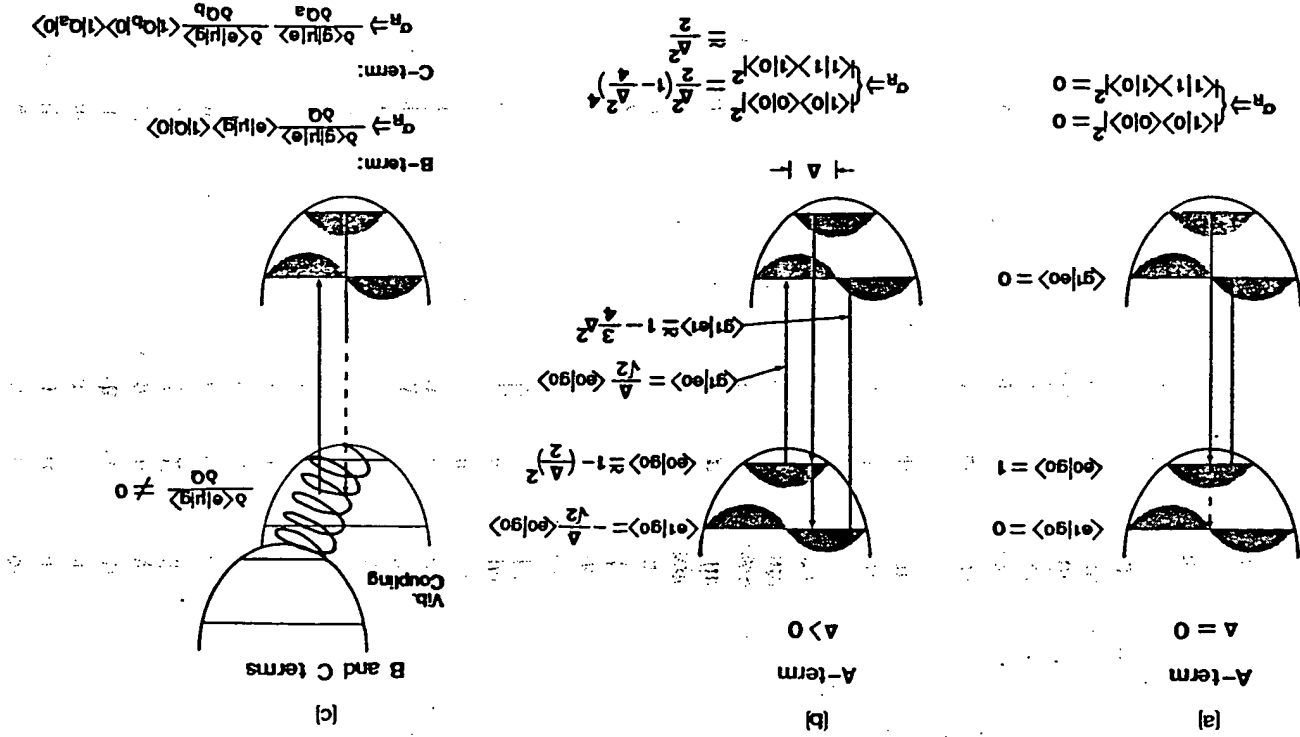
when the excited state vibrational states are solutions to a different Hamiltonian than that of the ground state. For the more common case of similar vibrational mode compositions in the ground and excited states, where the excited state geometry either expands or contracts relative to the ground state, the enhancement of totally symmetric vibrations scales roughly as  $\Delta^2/2$ , where  $\Delta$  is the magnitude of displacement of the excited state potential surface along the Raman active normal coordinate. For small displacements only the fundamental shows significant enhancement. Larger displacements result in lengthy Franck-Condon progressions. Thus, excited state geometry changes can be deduced from the pattern of internal coordinates active in the enhanced vibrations (43). Enhancement of symmetric vibrations by the *A*-term can also derive from vibrational force constant changes in the excited state, as well as by alterations in the composition of the excited state normal mode coordinates (Duschinsky effect). Although the *A*-term Condon mechanism dominates enhancement within strongly allowed transitions, Stallard et al (44) have demonstrated the importance of non-Condon contributions to enhancement of symmetric vibrations within the strong Soret band of ferro cytochrome c. Jones & Asher (45) also recently observed ca 15% non-Condon contributions to the enhancement of symmetric vibrations within the strongly-allowed electronic transition of myrcene.

Enhancement via the  $B$ -term derives from the non-Condon dependence of the electronic transition moment upon the vibrational coordinate. One example of a non-Condon enhancement mechanism is Herzberg-Teller vibronic coupling of different electronic transitions. Both symmetric and nonsymmetric fundamentals can be enhanced by a  $B$ -term mechanism. For a strongly allowed transition, the magnitude of  $B$ -term enhancement of symmetric vibrations is significantly below that for  $A$ -term enhancement.  $B$ -term enhancement will dominate only for the nonsymmetric vibrations. In contrast,  $B$ -term enhancement can dominate in transitions where significant oscillator strength derives from Herzberg-Teller coupling

to adjacent strongly allowed transitions (Figure 4). If the transition is rigorously forbidden at the equilibrium geometry, enhancement of fundamentals cannot occur via either the *A* or *B*-terms; however, *C*-term enhancement of overtones and combinations can occur, and will involve two quanta of vibrational mode *a*, or the combination of one quantum of mode *a* and one quantum of mode *b*. The *C*-term only dominates enhancement for resonance excitation within forbidden electronic transitions.

The energy denominators of the  $A$ ,  $B$ , and  $C$  terms cause individual electronic transitions to dominate the Raman cross-sections upon resonance excitation, provided that the spacing between adjacent transitions

**Figure 4** Pictorial rendition of  $A$  and  $B$  and C-term enhancement of a small excited state displacement mechanics (see Eq. (8). The important factors for enhancement are shown at bottom of figure where enhancement is assumed. A-term enhancement derives from large Franck-Condon overlaps in the upward and downward transitions, and dominances for symmetric vibrations in strong allowed transitions. As indicated in panels (a) and (b), A-term enhancement requires a displacement  $\Delta$ , for the excited state potential function relative to the ground state. If  $\Delta = 0$ , the Raman cross-section  $\sigma_R = 0$ . Otherwise  $\sigma_R \approx A^2/2$  for small excited state displacements. Non-Condon B-term enhancement (c) derives from the dependence of the transition moments upon vibrational motion. Both symmetric and nonsymmetric vibrations may show  $B$ -term enhancement. Panel (d) displays the Herzberg-Teller vibronic coupling mechanism where enhanced vibration coupling in an adiabatic strongly allowed transition. C-term enhancement occurs for forbIDDEN vibronic transitions that show no oscillator strength at the equilibrium intermediate geometry. Non-Condon coupling must occur for both the upward and downward electronic transition moment matrix elements.



is greater than the homogeneous linewidth,  $\Gamma_{vv}$ . Measurements of the dependence of the Raman cross-sections upon the excitation frequency, the Raman excitation profile (RREP), are particularly informative in studies of the dynamics of excited states.

A major simplification in the polarizability tensor expressions can occur in the preresonance region, where excitation occurs close to a dominating transition, but where the offset from resonance is large compared to  $\Gamma_{vv}$ . If one strong transition dominates, 4-term enhancement will dominate and the preresonance excitation profile of the Raman cross-sections for totally symmetric vibrations can be written (41, 46):

$$\sigma_{nm}^{\text{pre}} = 4\pi^2 \left( \frac{e^2}{\hbar c} \right) v_0 (v_0 - v_{nm})^3 g f(T) L(v_0) (10\Sigma^0 + 7\Sigma^2) \quad 9.$$

where  $\Sigma^0$  and  $\Sigma^2$  are defined by Eq. 5, but

$$\alpha_{vv} = \frac{2}{\hbar c} |\langle g | r_\rho | e \rangle|^2 \langle i | Q_a | f \rangle k_e \cdot \Delta \left( \frac{v_e^2 + v_0^2}{(v_e^2 - v_0^2)^2} \right) \quad 10.$$

where  $k_e$  is the vibrational force constant,  $\Delta$  is the displacement of the potential surface along the vibrational mode coordinate, and  $K$  is a collection of frequency-independent factors.

Equation 10 indicates that a measurement of the dispersion of the preresonance enhancement can be used to locate the transition frequency  $v_e$ . The magnitude of preresonance enhancement of a vibration is indicative of the magnitude of the displacement  $\Delta$  of the excited state potential surface along the vibrational mode coordinate.

Occasionally, one excited state does not completely dominate enhancement for excitation both far from resonance and well within the preresonance regime. This occurs because of the limited discrimination of the resonance energy denominators. Thus, the Albrecht *A*-term expression can be phenomenologically modified by adding a term to account for the contribution of states further from resonance (47, 48):

$$\alpha_{vv} = \frac{2}{\hbar c} |\langle g | r_\rho | e \rangle|^2 \langle i | Q | f \rangle k_e \cdot \Delta \left\{ \frac{v_e^2 + v_0^2}{(v_e^2 - v_0^2)^2} \right\} + K_2. \quad 11.$$

Although this additional term ( $K_2$ ), alone, gives a frequency-independent contribution to  $\alpha_{vv}$ , it results in an additional frequency dependence in

$|\alpha_{vv}|^2$  due to the interference term with the first frequency-dependent term of Eq. 11 (48).

The expressions above are used to model the measured Raman cross-sections. The RREP data, the depolarization ratios, and the normal mode compositions of the enhanced vibrations can be combined to determine excited state geometry changes, and to monitor dynamical coupling among electronic, vibrational, and rotational motions.

## APPLICATIONS

The applications discussed are chosen from studies that incisively utilize the unique capabilities of UVRR spectroscopy. I attempt to review the current activities in UV Raman spectroscopy and conclude this review by discussing two new techniques that are likely to make major contributions to the understanding of molecular structure and dynamics in the near future. These techniques are Saturation Raman Spectroscopy and Resonance Hyper-Raman Spectroscopy.

As discussed in detail toward the end of the review, Saturation Raman Spectroscopy (49a,b) examines the rate of recovery of molecules back to the ground state after photon absorption transfers these molecules into an excited state during a resonance Raman measurement. The rate of ground state recovery depends upon molecular structure and environment.

Resonance Hyper-Raman Spectroscopy (50–52) is a second-order process where excitation with light of frequency  $v_0$  results in Raman scattering at  $2v_0 - v_v$ , where  $v_v$  is a vibrational mode frequency. A two-photon resonance occurs with electronic transitions centered at  $2v_0$ , to enhance the cross-sections of the Hyper-Raman bands. Although visible wavelength excitation is used, the technique probes far UV electronic transitions.

The intense activity in UV Raman studies of molecular excited states and dynamics can be categorized into three different types of studies. (a)

studies that utilize Raman intensities and bandwidths to resolve excited state dynamics, especially within photodissociating electronic transitions;

(b) studies that probe excited state structure by relating the Raman cross-sections to changes in excited state geometry; (c) studies that utilize the selectivity of UV Raman enhancement to examine molecular structure in complex systems.

## Dynamical Studies

The recent study of  $\text{CH}_3\text{I}$  photodissociation by Imre et al (38–40) examined Raman scattering excited in resonance within a dissociating electronic transition. By using Heller et al's (36, 37) time-dependent formalism, the relative Raman intensities of the fundamentals and overtones were used

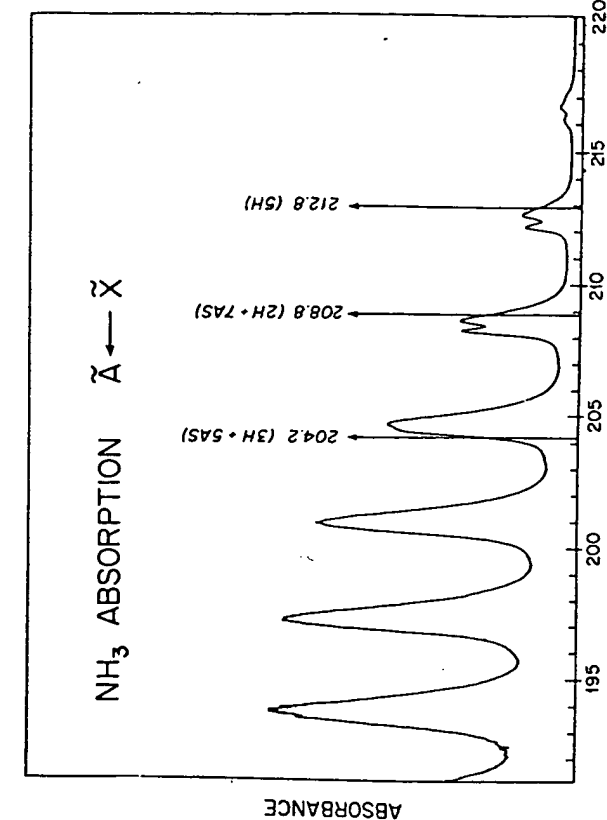


Figure 5. Absorption spectrum of  $\text{NH}_3$  gas at room temperature. Arrows indicate excitation wavelengths. From Ref. (56).

to gain quantitative information upon molecular excited state structure, the nature of the electronic potential surfaces, and the dynamics of the photodissociation process. This time-dependent formalism derives from the inverse LaPlace Transform of the KHD expressions and is simply a restatement of second order perturbation theory in the time domain. This formalism, which is not reviewed here, has the advantage that it is cast in the time domain, and unique physical insight can be obtained on probabilistic short-time dynamics of a photodissociative process.

The  $\text{CH}_3\text{I}$  studies of Imre and the Kinsey group (38–40), and the  $\text{NO}_2$  studies of Rohlffing & Valentini (53), clearly illustrate the dynamical information available from the relative Raman intensities. The relative  $\text{CH}_3\text{J}$  fundamental and overtone Raman intensities were used to determine the magnitudes of the slopes (the forces) of the potential surface along the stretching and bending molecular coordinates. The Raman intensities report upon the shape of the excited state potential surfaces and the probability density surface for photodissociation. Indeed, because of the dependence of the Franck-Condon overlap factors on the relative shifts between potential surfaces, the intensities of the higher overtones are determined selectively by the dissociating edge of the excited state potential surface. In contrast, the intensities of the fundamentals are dominated by the potential surface located around the ground state equilibrium nuclear geometry. As a result, the fundamentals and overtone intensities report on short and longer time dynamics, respectively (i.e. approximately less than and greater than one ground state vibrational period). These types of studies are uniquely informative of the likely trajectories of photo-dissociating molecules. It is likely that these methods will be applied to study other photodissociating systems.

Ziegler et al (54–58) adopted a different approach to examine dynamics of photodissociation in gaseous and condensed phase solutions of  $\text{NH}_3$ . They carefully examined the resonance Raman spectra and excitation profiles of the 160–220 nm  $A \leftarrow X\text{NH}_3$  transition (Figure 5). This Rydberg transition, which is associated with promotion of a nitrogen lone pair electron to a  $3s$  Rydberg orbital, shows a long progression in the gas phase in the  $v_2$  umbrella bending coordinate. The gas phase absorption bands are broad due to lifetime broadening (greater than  $100 \text{ cm}^{-1}$  linewidths), and no rotational fine structure is observed. In the condensed phase these bands severely weaken and broaden. Excitation into this state in the gas phase results in photodissociation to  $\text{NH}_2$  and  $\text{H}$  with a quantum yield of unity; the homogeneous linewidth or dephasing rate,  $(1/\Gamma_{ev})$ , for this transition is dominated by the photodissociation rate. Resonance Raman excitation into the vibronic subbands show progressions in the  $v_2$  out-of-plane umbrella bending coordinate, since the pyramidal ground state

becomes planar in the photodissociating excited state. In addition strong enhancement is observed for  $v_1$ , the symmetric stretching coordinate. Careful examination of the rotational structure in the UVRR spectra clearly reveals that the lifetime of the dissociating excited state is a function of both the vibronic and rotational energy levels. As indicated in Eq. 8, the Raman cross-section depends upon the homogeneous linewidth parameter,  $\Gamma_{ev}$ , which is related to the reciprocal of the excited state lifetime. These expressions were written for vibrational Raman scattering, and can be readily extended to rovibronic scattering (where the rotational states are separable) by including the rotational states and by recognizing the rotational state dependence of the energy denominators. Ziegler has calculated the required expressions that can be used to model the relative rovibronic Raman intensities (56). Since  $\text{NH}_3$  can be modeled well as a symmetric top, the only unknown parameter within the rigid rotor approximation is the homogeneous linewidth, which, as described above, is related to the dissociation rate. Qualitatively, the shorter the lifetime the more rotational transitions will be resonantly enhanced and observed, since their offset from resonance will become comparable to or less than  $\Gamma_{ev}$ , the bandwidth. In contrast, longer lifetimes will result in a smaller  $\Gamma_{ev}$

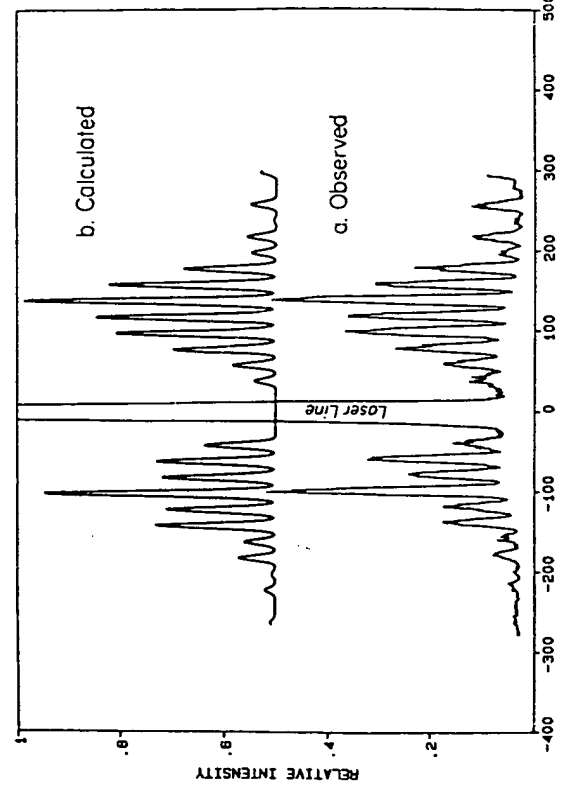


Figure 7 Comparison of observed and calculated resonance rotational Raman spectrum of  $\text{NH}_3$  with 208.8 nm excitation. The calculated spectrum derives from the use of an excited state lifetime of 93 fsec ( $\Gamma = 55 \text{ cm}^{-1}$ ). From Ref. (56).

and a sharper resonance, which will give rise to resonance Raman spectra with fewer calculated rotational transitions. Indeed, Figure 6 illustrates the dependence of the rotational structure upon excited state lifetime for 208.8 nm excitation of  $\text{NH}_3$ , and Figure 7 shows the agreement possible between the observed and calculated spectra. Obviously, the spectra are extraordinarily sensitive to lifetime, which permits Ziegler to conclude that the ammonia excited state lifetime decreases from 140 fsec in the  $v_2 = 1$  vibronic level to 56 fsec in the  $v_2 = 3$  vibronic level.

Ziegler also demonstrated (57) a rotational state dependence for photo-dissociation by examining the UV rotational excitation profiles through the  $v'_2 = 2$  vibronic absorption band. The rotational state dependence of the dissociation rate is obtained directly from the excitation profile, since the only unknown parameter is the excited state lifetime. Figure 8 shows the  $R$  and  $S$  rotational transitions accompanying the  $v_1 + v_2$  combination band as a function of excitation within the  $v'_2 = 2$  vibronic subband; Figure 9 shows the measured and calculated excitation profiles. As indicated in Table 1 the rovibronic lifetimes and rates strongly depend upon the

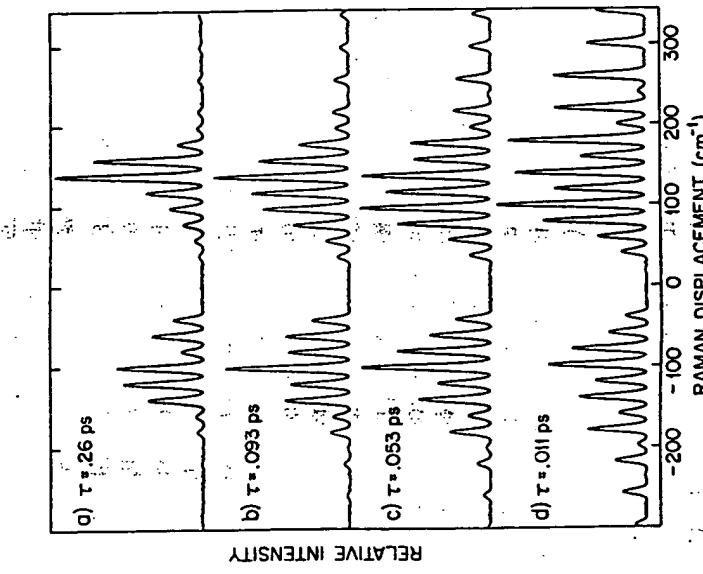


Figure 6 Dependence of the calculated  $\text{NH}_3$  resonance Raman rotational structure upon excited state lifetime for 208.8 nm excitation where  $\tau = (2\pi\Gamma_{\text{ex}})^{-1}$ . From Ref. (56).

Table 1 Rovibronic lifetimes and photodissociation rates determined by  $S$  and  $O$  RRREPs for the  $v'_2 = 2$  absorption band of the  $X \rightarrow A$  transition of  $\text{NH}_3$

Raman transition	Initial $J$	Resonant $J'$	$\Gamma$ (fsec) <sup>a</sup>	$\Gamma$ (fsec) <sup>a</sup>	Rate $\times 10^{-12} \text{ s}^{-1}$
$S$	1	2	141	7.1	
	2	3	100	10.0	
	3	4	91	11.0	
	4	5	78	12.7	
	5	6	75	13.3	
	6	7	70	14.3	
	7	8	68	14.7	
	8	2	139	7.2	
$O$	3	2	109	9.2	
	4	3	111	9.0	
	5	4	102	9.8	
	6	5	91	11.0	
	7	6	82	12.2	
	8	7			

<sup>a</sup>Absolute lifetime error is estimated to be  $\pm 10\%$ . Relative lifetime error is  $\pm 5\%$ . From Ref. (57).

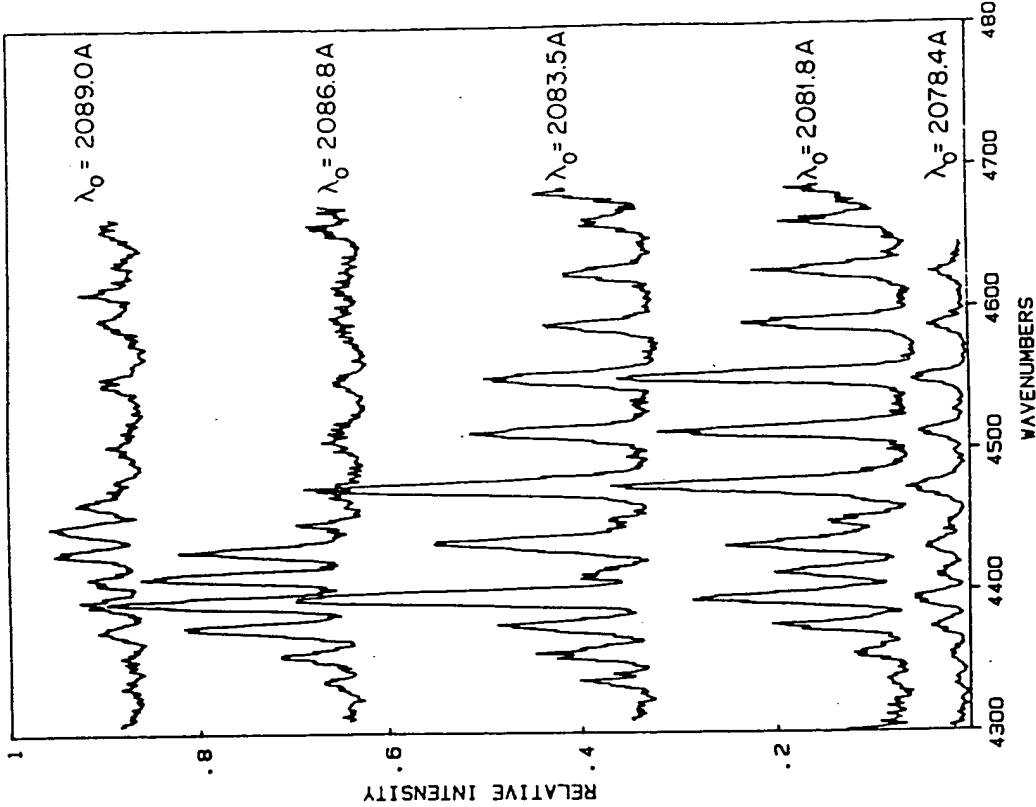


Figure 8 Resonance enhanced *R* and *S* transitions accompanying the  $v_1 + v_2$  combination band of  $\text{NH}_3$ . The displayed intensities are normalized to the internal standard  $v_1$  band of methane. From Ref. (57).

rotational levels involved. The lifetimes decrease from 151 fsec for  $S1$  ( $J = 1, J' = 2$ ) to 68 fsec for  $S7$  ( $J = 7, J' = 8$ ). Similar lifetime decreases are observed for the  $O$ ,  $P$ , and  $R$  Raman transitions. It is interesting that the photodissociation rates appear to depend upon how the upper state is populated; the rates differ between  $S$  and  $O$  transitions that terminate in identical  $J'$  levels.

Thus, the intramolecular dissociation rates are strongly dependent upon the angular momentum of the populated states. Ziegler suggests that this rotational state dependence derives mainly from centrifugal effects on the quasibound  $A$  state surface and that higher resolution RREP studies will be used in the future to explore the relative contribution of Coriolis coupling to increasing the dissociation rate. These studies monitor the dynamics of photodissociation and detail the role of rotations in determining the dissociation rate constants.

The dissociation dynamics present in the gas phase are expected to be greatly modified in the condensed phase. Indeed, Rydberg transitions become weaker and more diffuse when a molecule such as  $\text{NH}_3$  is placed in solution. Recently Ziegler & Roebber examined  $\text{NH}_3$  dissolved in hexane and observed that the  $v_2$  stretching Raman cross-section was decreased relative to that in the gas phase (58). This decrease was suggested to derive from an increased dephasing rate of the Rydberg transition due to coupling with low frequency solvent bath modes. These types of studies are crucial to establish connections between the vibronic transitions of gas phase molecules and those in solution. Careful establishment of these connections is especially important for higher energy transitions where host matrix transitions exist at energies similar to those of the solute.

We recently observed similar homogeneous linewidth differences upon excitation into the  $B_{2u}$  vibronic bands of gas and solution phase benzene (59–61). In solution, little enhancement derives from the  $B_{2u}$  vibronic components because of their large homogeneous linewidths. In the gas phase these transitions give strong resonance enhancement due to their narrow  $3 \text{ cm}^{-1}$  linewidths (60). Indeed, the resonance Raman cross-section maxima should show a  $\Gamma^{-2}$  dependence upon homogeneous linewidth.

By examining the details of the excitation profile of the  $v_1$  band near one of these narrow vibronic resonances, we were able to probe the excited state dephasing dynamics (60). Figure 10 shows that benzene Raman spectra excited at 43,170, and 43,280  $\text{cm}^{-1}$  are dominated by the symmetric  $v_1$  ring and  $v_2$  C–H stretching vibrations. The Raman cross-sections of benzene were measured relative to the known cross-sections of the internal standard methane (62); the C–H methane stretching band occurs at 2920

$\text{cm}^{-1}$ . The Raman excitation profiles (Figure 11) measured between 19,000 and 45,000  $\text{cm}^{-1}$ , excited away from resonance with  $B_{2u}$  vibronic features, monotonically increase with increasing excitation frequencies (Figure 11). The use of the modified *A*-term expression (Eq. 11) indicates that the

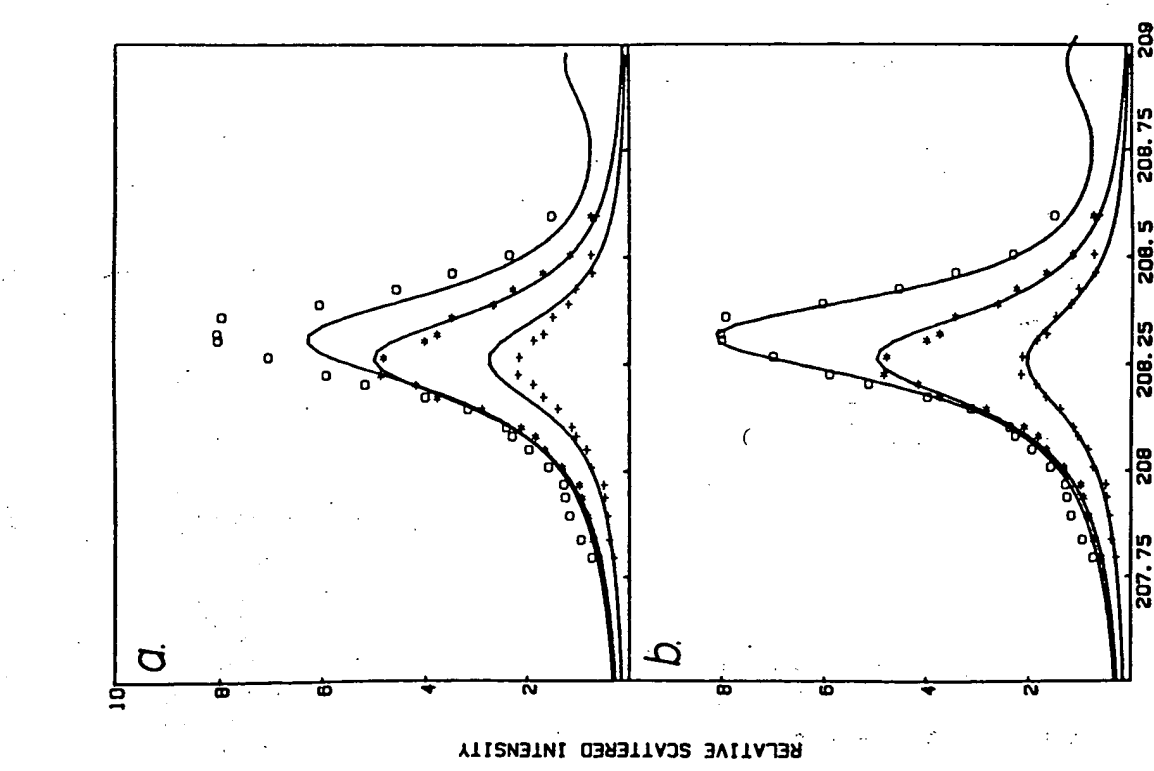


Figure 9 (a) RREP for the S3(○), S5(\*), and S7(+) transitions of  $\text{NH}_3$ . Solid curves calculated with  $\Gamma = 68 \text{ cm}^{-1}$ . (b) Best fit to the S3, S5, and S7 RREP give  $\Gamma = 56, 68$ , and  $75 \text{ cm}^{-1}$ , respectively. From Ref. (57).

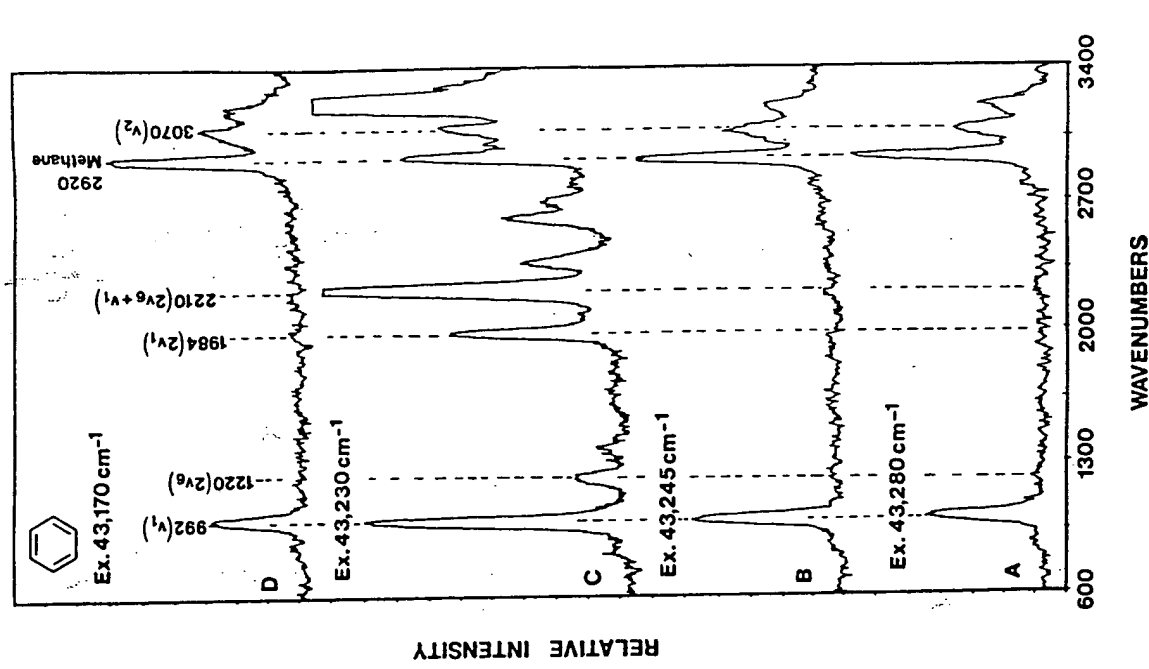


Figure 10 Raman spectra of gas phase benzene obtained with excitation in the vicinity of the  $B_{2u} 6_o^3$  transition. The benzene bands are labeled and the intensities are determined by reference to the methane internal standard band at  $2920 \text{ cm}^{-1}$ . The spectra were obtained at the excitation frequencies shown in the inset of Figure 11. From Ref. (60).

enhancement of the  $\nu_1$  band derives almost entirely from the  $E_{1u}$  and  $B_{1u}$  transitions at higher energy. Excitation studies by Gerrity et al (63) directly into the  $E_{1u}$  transition show strong  $\nu_1$  enhancement by the  $E_{1u}$  transition, but destructive interference with excitation between the  $B_{1u}$  and  $E_{1u}$  transitions (200 nm).

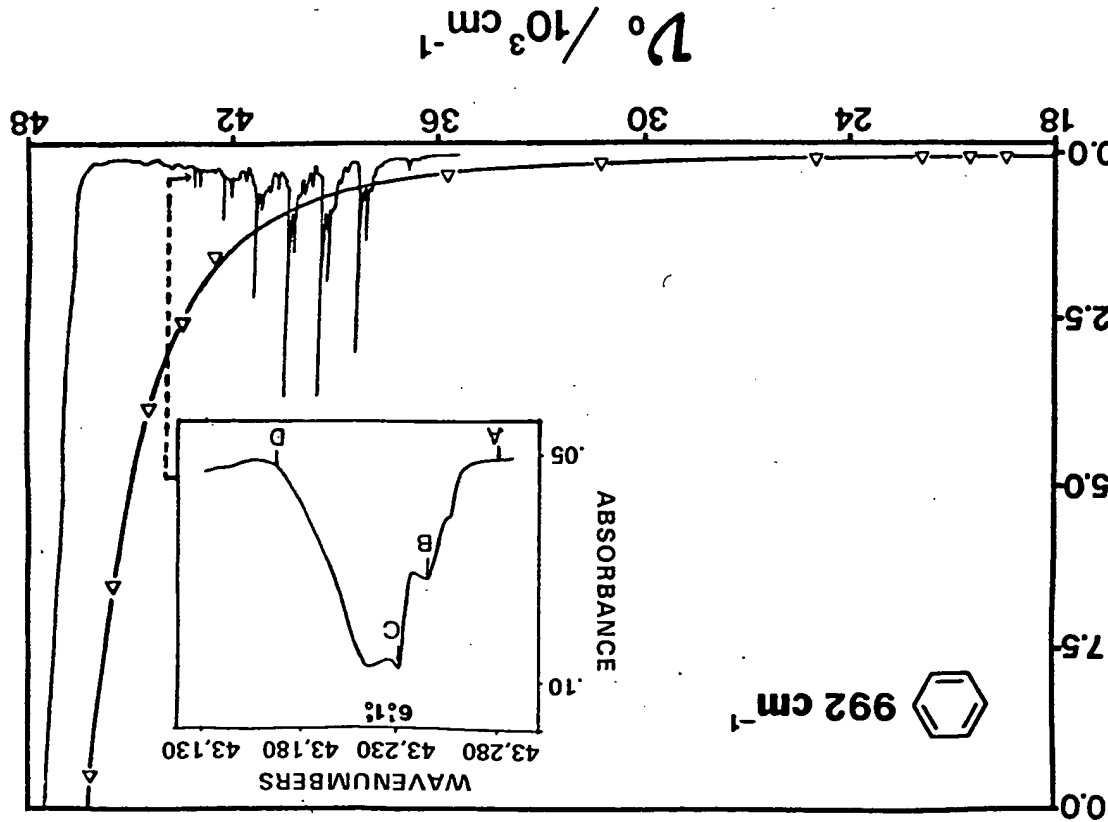
Figure 10, which shows the 43,230  $\text{cm}^{-1}$  excited resonance Raman spectrum within the  $6'_0 1'_0 B_{2u}$  vibronic transition, shows enhancement not only of  $\nu_1$  but also of  $2\nu_1$ , and additional harmonics. In addition, a  $2\nu_6$  band is observed as well as its combinations with  $\nu_1$ . The progressions in  $\nu_6$  clearly derive from the C-term scattering mechanism, where a one-quantum change occurs for both the upward and downward Raman transitions; the strictly forbidden  $B_{2u}$  transition obtains oscillator strength mainly through Herzberg-Teller coupling by the  $\nu_6$  vibration.

The excitation profile of the  $\nu_1$  vibration can be used to examine dephasing, since the magnitude of interference between the preresonance Raman and resonance Raman scattering will decrease as the dephasing time shortens. In the absence of pure dephasing all of the emission is Raman and interference is a maximum. Fast pure dephasing results in resonance emission that derives mainly from hot luminescence (HL) (otherwise known as single vibrational level fluorescence, SVLF) that does not add at the amplitude level (polarizability level) to the preresonance Raman intensities. Prior to pure dephasing the resonance Raman excitation profile in the  $B_{2u}$  absorption feature will show constructive and destructive interference with the preresonance contribution as excitation passes through resonance; the energy denominator of Eq. 8 passes through zero to alter the sign of resonance Raman polarizability. In contrast, if emission occurs subsequent to dephasing and occurs from a molecular eigenstate, the SVLF or HL will contribute independently of the pre-resonance Raman intensity (see Figure 12).

Figure 13, which shows the RREP through the  $6'_0 1'_0$  benzene vibronic absorption band, shows the presence of constructive and destructive interference in the RREP, and indicates that some resonance Raman emission occurs prior to pure dephasing. Quantitative modeling reveals that about 50% of the  $\nu_1$  resonance emission intensity derives from SVLF or HL. We determined a ca 2 psec pure dephasing time. By examining the pressure dependence of the Raman intensities we were able to identify this ca 2 psec dephasing process as intramolecular vibrational redistribution (IVR) and were able to estimate the number of levels coupled by the IVR process. The presence of SVLF was also signaled by the observed depolarization ratios, which increased to  $\rho = 1$  as the emission lifetime became larger than the rotational period.

As experimental resources increase for UV Raman measurements it is

Figure 11 Gas phase benzene absorption spectrum and RREP of the 992  $\text{cm}^{-1}$  symmetric ring breathing vibration. Inset shows details of the 43,200  $\text{cm}^{-1}$  absorption region. From Ref. (61).



$$\frac{\rho_{\text{mm}}}{\text{mBar}} \left( \frac{\text{mol}}{\text{mol} \cdot \text{str}} \right)$$

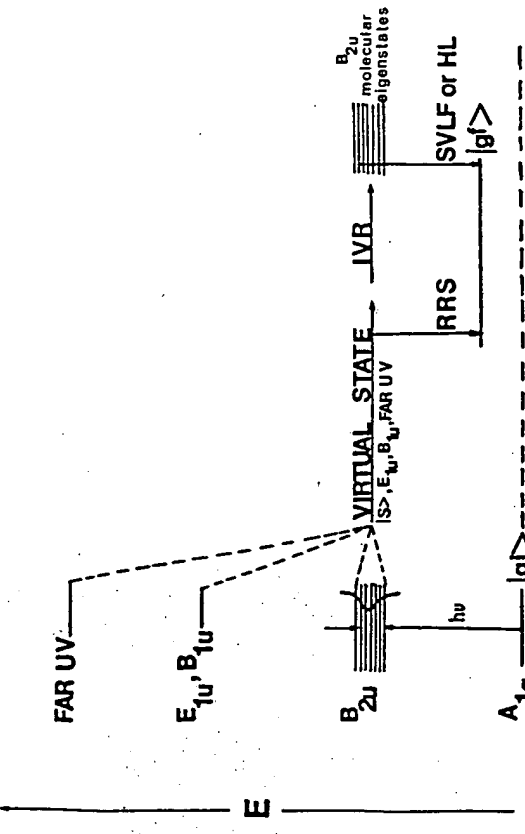


Figure 12 Schematic diagram of RRS, HI, and SVLF. Closely spaced horizontal lines represent  $B_{2u}$  molecular eigenstates. The superposition or virtual state, which gives rise to RRS and the interference effects, contains contributions from resonant and preresonant states. Intramolecular vibrational redistribution (IVR) dephases the superposition state and populates the  $B_{2u}$  molecular eigenstates. Emission from the eigenstates is HL (or SVLF). From Ref. (60).

certain that additional studies will examine dynamics of photodissociation and photochemistry and the dephasing of the coherent states prepared by the radiation field.

#### *Studies of Electronic Excited States*

The study of molecular excited states by Raman spectroscopy involves the investigation of the relative enhancement and the depolarization ratios of different vibrational modes. The depolarization ratios identify which invariants of the polarizability contribute. In resonance the depolarization ratio for symmetric vibrations will uniquely determine whether an electronic transition is polarized along a single direction, whether differently polarized electronic transitions overlap, or whether degeneracy is present. The relative enhancement of vibrations is directly diagnostic of geometry or force constant changes in the excited state. Since the magnitude of the Franck-Condon factors for the fundamental of a symmetric vibration is directly related to the displacement of the excited state potential surface along that vibrational coordinate, the magnitudes of enhancement can be

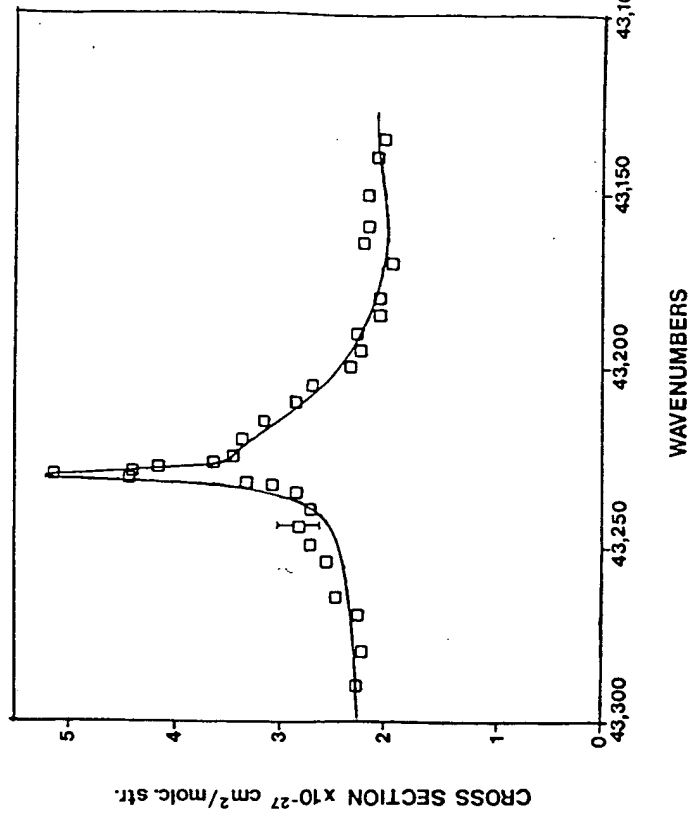


Figure 13 Raman excitation profile of the  $992\text{ cm}^{-1}$  benzene ring vibration within the  $B_{2u} 6_0^1 3$  vibronic transition. The solid curve is the calculated excitation profile assuming almost equal contributions of resonance Raman and SVLF emission. This leads to a ca. 2 ps dephasing time. From Ref. (60).

used to determine quantitatively the geometry change within the basis set of the symmetric normal mode coordinates (Figure 4).

RREP can also be used to identify underlying vibronic band structure or overlapping transitions. Obviously, dispersion of the depolarization ratios conveys additional information. Preresonance excitation profiles can be used to identify the location of higher energy transitions, and the relative preresonance enhancements of different vibrations can be used to probe qualitatively the geometry changes in preresonant excited state.

Preresonance Raman studies are especially useful for the identification of far UV electronic transitions. As clearly pointed out in the insightful volumes of Robin (64), the vacuum UV region is relatively unexplored, with few transitions clearly identified or characterized even for the simplest gas phase molecules. The information on vacuum UV transitions available for molecules in the condensed phase is truly "underwhelming."

Fitting the RREP data using the *A*-term expression (Eqs. 10 and 11)

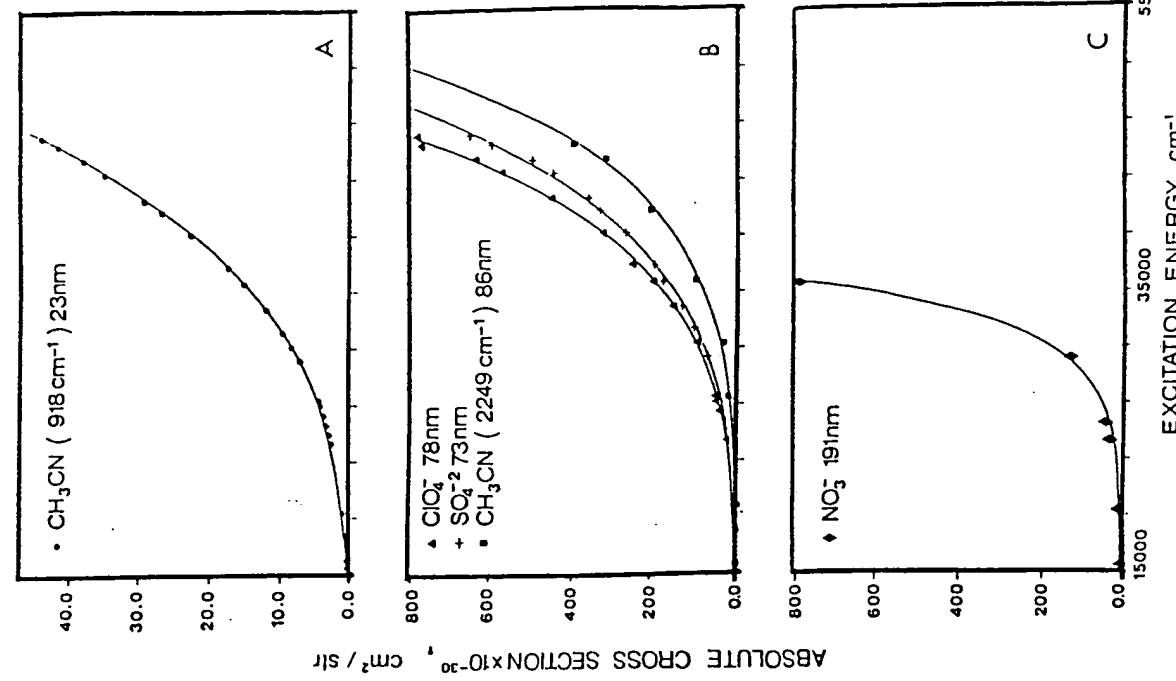


Figure 14 Total differential Raman cross-sections of (A) the  $918 \text{ cm}^{-1}$  C-C stretch of acetone, (B) the  $2249 \text{ cm}^{-1}$  C≡N stretch of acetonitrile, the  $932 \text{ cm}^{-1}$  symmetric stretch of  $\text{ClO}_4^-$ , and the  $981 \text{ cm}^{-1}$  symmetric stretch of  $\text{SO}_4^{2-}$ . (C) The  $1045 \text{ cm}^{-1}$  symmetric stretch of  $\text{NO}_3^-$ . The solid lines show A-term expression best fit to Eq. 10. From Ref. (31).

will extract the transition frequency of the preresonant transition. The maximum preresonance enhancement occurs for symmetric vibrations with major contributions from those internal vibrational coordinates that project along the coordinates of the excited state geometry change. Thus, excitation even out of resonance allows information to be obtained on transitions further in the UV. Often, direct absorption measurements of these transitions are impossible due to interference from overlapping solvent transitions. All solvents show absorption interferences below ca 180 nm.

Preresonance Raman studies have recently appeared for species such as acetone (48),  $\text{CH}_3\text{CN}$  (31), acetamide and *N*-methylacetamide (48),  $\text{ClO}_4^-$  (31),  $\text{SO}_4^{2-}$  (31), 1-cystine (65), imidazole (66), and water (66). We developed a new technique to determine the dispersion of Raman cross-sections in the UV and examined species that were useful as internal intensity standards for future UV measurements (31). The absolute scaling of the cross-sections was obtained by referencing our relative cross-sections to the 514.5 nm benzene absolute differential Raman cross-sections of Abe et al (35). Measurements of gas phase Raman cross-sections are more straightforward, and Black & Bischel (62) have reported cross-section measurements for  $\text{CH}_4$ ,  $\text{D}_2$ ,  $\text{H}_2$ ,  $\text{N}_2$ , and  $\text{O}_2$  from the visible spectral region into the UV (below 200 nm).

Figure 14 shows the dispersion of the cross-sections of the C-C stretch ( $918 \text{ cm}^{-1}$ ) and the C-N stretch ( $2249 \text{ cm}^{-1}$ ) of  $\text{CH}_3\text{CN}$ , and the symmetric stretches of  $\text{ClO}_4^-$ ,  $\text{SO}_4^{2-}$ , and  $\text{NO}_3^-$  ions in aqueous solution. The solid lines show A-term fits to the preresonance cross-section data. The  $\text{NO}_3^-$  preresonant cross-sections are accurately modeled by the simple A-term expression, which indicates that the enhancement derives from a transition at  $191 \text{ nm}$ , which is close to the well known  $200 \text{ nm}$   $\pi \rightarrow \pi^*$  transition. Thus, for  $\text{NO}_3^-$  preresonance enhancement derives solely from a UV state that undergoes an expansion along the N-O bonds.

In contrast, the C-C stretch of  $\text{CH}_3\text{CN}$  shows almost no preresonance enhancement, as evident from the extrapolation of its preresonance transition to  $25 \text{ nm}$ . Indeed, extraordinarily high energy preresonance transitions are derived from A-term fits for  $\text{CH}_3\text{CN}$ , sulfate,  $\text{ClO}_4^-$ , acetone,  $\text{H}_2\text{O}$ :  $86 \text{ nm}$  for the C≡N stretch of  $\text{CH}_3\text{CN}$ ,  $73 \text{ nm}$  for the symmetric stretch of sulfate ion,  $78 \text{ nm}$  for the symmetric stretch of  $\text{ClO}_4^-$ ,  $80 \text{ nm}$  for the carbonyl stretch of acetone, and  $68 \text{ nm}$  for the  $1645 \text{ cm}^{-1}$  bending vibration of water.

These extrapolated transition frequencies are surprisingly high relative to naive expectations, since most workers assume that strong acetonitrile and acetone C≡N and C=O  $\pi \rightarrow \pi^*$  transitions occur in the  $150$ – $180 \text{ nm}$  spectral region (31, 64). These transitions should result in significant C–N

and C–O bond elongations, which would lead to strong enhancements. Similar expectations exist for  $\text{SO}_4^{2-}$  and  $\text{ClO}_4^-$ , which display absorption edges at ca 180 nm, and broad intense features are observed below 160 nm. Our perusal of the vacuum UV literature had lead us to the realization that no clear assignment exists for the acetone  $\pi \rightarrow \pi^*$  transition, nor is there a clear understanding of the absorption spectra of  $\text{SO}_4^{2-}$  and  $\text{ClO}_4^-$  ions in water. Charge transfer transitions between the ions and water have been suggested to be important for  $\text{SO}_4^{2-}$  and  $\text{ClO}_4^-$  absorption bands. Indeed, the relevant question is whether molecular transitions are even likely to exist in the vacuum UV spectral region, where the density of states is so high and where intermolecular transitions (charge transfer) are likely to dominate the oscillator strengths. These UV Raman measurements are expected to serve as a sensitive probe for the existence and importance of vacuum UV electronic transitions.

In general, preresonance RREP of species with well-resolved, clearly assigned UV transitions show satisfactory  $A$ -term fits giving expected transition frequencies. Examples include imidazole (66), acetamide, and *N*-methylacetamide (48). Figure 15 shows the visible and UV Raman spectra of *N*-methylacetamide, while Figure 16 shows the preresonance RREP for these bands. Prominent bands observed include the Amide I, II, and III bands, which are dominated (see Figure 15) by carbonyl stretching (Amide I), and C–N stretching and C–H bending (Amide II and III). The 1162, 881 and 628  $\text{cm}^{-1}$  bands each contain major contributions of either C–C stretching or N–CH<sub>3</sub> rocking in addition to NCO bending. As evident in the simple one-state  $A$ -term fits shown on the left side of Figure 16, an excellent modeling occurs for the Amide II and III bands which are dominated by C–N stretching. The preresonant state is extrapolated to occur at 185 nm, the location of the well-known amide  $\pi \rightarrow \pi^*$  transition. In contrast, less acceptable fits occur for bands with appreciable C–C stretching and NCO bending. The inability to fit simultaneously the visible and UV Raman RREP for these bands indicates that more than one transition is important to their preresonance enhancement. The 185 nm  $\pi \rightarrow \pi^*$  transition does not completely determine the enhancement of bands with appreciable C–C stretching and NCO bending. The RREP of the Amide I band, which is dominated by C–O stretching and shows little enhancement by the 185 nm transition, is not plotted because it overlaps the Amide II band. We conclude that the  $\pi \rightarrow \pi^*$  transitions of amides involves large C–N bond elongation. This result is important because it argues against theoretical calculations that predict a larger C–O than C–N bond order change for the  $\pi \rightarrow \pi^*$  transition (67, 68). Further, we have recently tentatively assigned the 1496  $\text{cm}^{-1}$  *N*-methylacetamide band to the overtone of the Raman-forbidden Amide V torsional vibrational (68a).

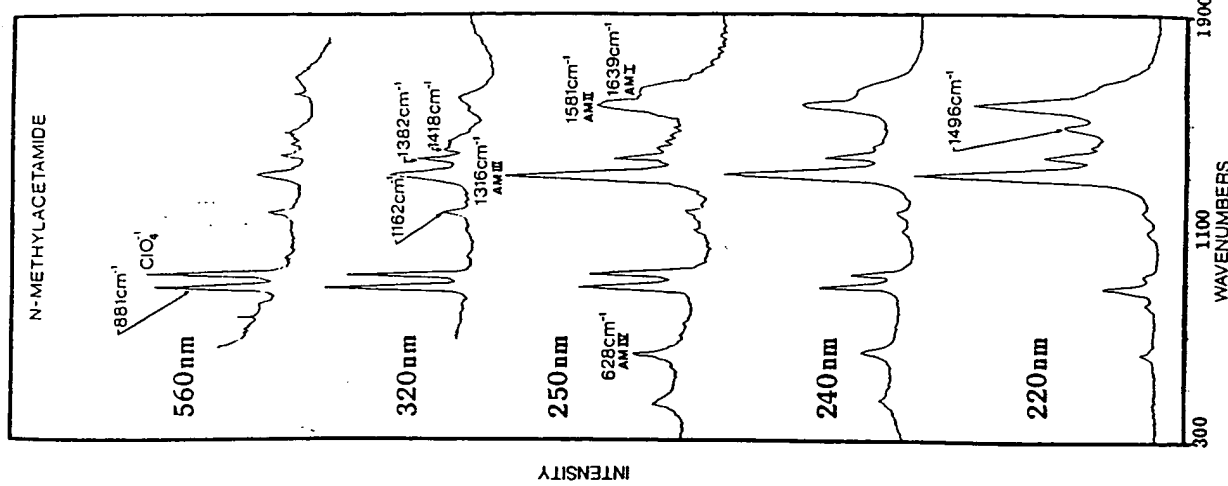


Figure 15 Raman spectra of aqueous solutions of *N*-methylacetamide. The internal standard perchlorate (0.2 M) contributes the 932  $\text{cm}^{-1}$  band. *N*-methylacetamide concentrations were 1.0 M for 560 nm and 320 nm excitation, and 0.4 M for the other excitation wavelengths. From Ref. (48).

N-METHYLACETAMIDE  
STANDARD A-TERM  
MODIFIED A-TERM

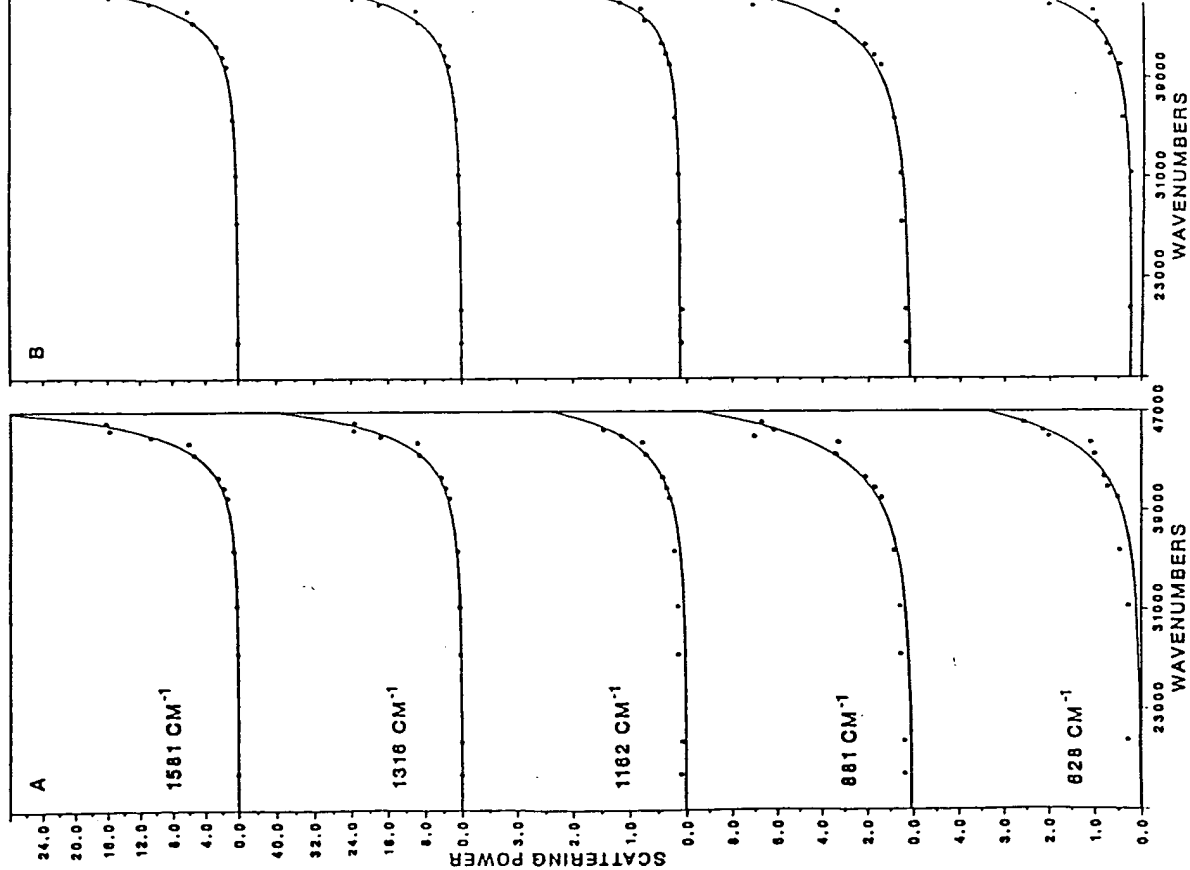


Figure 16 Preresonance RREP of *N*-methylacetamide. The solid curve in the left-hand panel corresponds to a best fit with the *A*-term expression given by Eq. 10, while the right-hand panel shows the best fit to the modified *A*-term expression given by Eq. 11. From Reibis (imidazole) Fe(III) protoporphyrin IX-dimethylester, a model for the

The anomalous enhancement of this band by the Amide  $\pi \rightarrow \pi^*$  transition suggests that the excited state is twisted in a manner similar to that of ethylene (*vide infra*).

The enhancement pattern for *N*-methylacetamide is drastically changed by deuteration, as shown recently by Mayne et al (69). The increased deuterium mass results in decoupling of N-H bending from C-N stretching for the Amide II and III modes, and an Amide II' band replaces the Amide II and III bands. This Amide II' vibration is almost a pure C-N stretch, and shows a cross-section almost the sum of that of the Amide II and III bands. Thus, the Raman cross-sections quantitatively report upon the magnitude of the projection of the normal coordinate upon the excited state geometry changes. A similar decoupling of C-H bending and C-N stretching occurs for proline derivatives, which leads to dramatic enhancement of a similar Amide II' band for these molecules (70-72).

The excited states of numerous small gas phase molecules such as ethylene (76a,b), and derivatives such as dichloro and dimethylethylene (42), butadiene (77), CS<sub>2</sub>(78), benzene (9, 10, 47, 60, 61, 63), and styrene (79), have been probed with UV Raman excitation. Studies of ethylene in the  $N \rightarrow V$  transition (ca 190 nm) show enhancement of even overtones of the  $a_u$  torsional mode, which indicates that the excited state is twisted with respect to the planar ground state (76a,b). Large enhancements are also observed for C-C stretching and CH<sub>2</sub> scissoring motions, which indicate an increased C-C bond length and decreased CH<sub>2</sub> bond angles in the excited state. The increased C=C bond length presumably derives directly from a bond order decrease. The decreased C-H bond angle probably derives from the increased carbon sp<sup>3</sup>-like hybridization in the excited state.

Studies of styrene with excitation in its S<sub>2</sub>, S<sub>3</sub>, and S<sub>4</sub>  $\pi \rightarrow \pi^*$  transitions between 190 and 260 nm examined the relative enhancement of the ring vibrations compared to the vinyl group stretching, angle bending, and torsional motions (79). In contrast to ethylene, no vinyl group torsional modes were enhanced, thus indicating a much larger barrier to twisting in the excited state of styrene compared to ethylene. The enhancements observed for the ring modes and vinyl stretching were similar for excitation in the S<sub>2</sub> and S<sub>3</sub> transitions, a result that indicates the delocalized nature of the ground and/or the excited S<sub>2</sub> and S<sub>3</sub> states. The S<sub>1</sub> transition is known to be localized on the ring from absorption and fluorescence measurements. Excitation into S<sub>4</sub>, however, results mainly in enhancement of bands that are predominantly ring vibrations; the nature of this excited state appears very reminiscent of the benzene E<sub>1u</sub> transition.

We have recently concluded a study (80) of the electronic transitions of bis(imidazole) Fe(III) protoporphyrin IX-dimethylester, a model for the

vinyl stretching becomes enhanced via an *A*-term mechanism. Thus, these UV Raman measurements can determine the extent of delocalization of orbitals associated with substituents attached to aromatic ring systems and can be used to probe delocalization of the resonant excited state. Further, the extent of vinyl orbital delocalization should be sensitive to the vinyl group orientation with respect to the heme ring.

### Biophysical and Analytical Applications

The Amide band frequencies and intensities are important markers of protein and peptide backbone folding and conformation (73, 74). Because of exciton interactions, the amide  $\pi \rightarrow \pi^*$  transition dipoles can add constructively or destructively. For example, the  $\alpha$ -helix conformations show a ca 40% hypochromic oscillator strength decrease compared to random coil or  $\beta$ -sheet. This oscillator strength decrease is accompanied by a greater than 60% decrease in the Amide II and III band cross-sections. In contrast, the Amide I band shows only a modest alteration in Raman cross-section. Spiro et al (71, 74, 75a,b) have begun to utilize this conformational dependence for the UV Raman intensities for protein structural studies. They recently demonstrated linear correlations between amide mode cross-sections and the protein peptide conformation (75a,b).

Numerous other studies have recently focused upon the protein aromatic amino acids (12, 13, 18, 19, 49a,b, 74, 84-89) in order to clarify the enhancement phenomena and to determine the selectivity available for enhancement of these residues in proteins. Important mechanistic information may derive from RR measurements that selectively excite those aromatic amino acid residues important in the protein enzymatic reaction coordinate. The vibrational mode frequencies and cross-sections will report on the aromatic amino acid residue environment. For example, the frequencies will depend upon hydrogen bonding. An environmental cross-section dependence occurs because the absorption band oscillator strength and its homogeneous and inhomogeneous linewidths depend upon the environment. In addition, the Raman cross-sections depend upon the local field, which varies as the effective refractive index of the environment surrounding a residue changes. Careful studies of the environmental dependence of the aromatic amino acid band frequencies and cross-sections are just now underway (25, 88, 89).

The major impediment to these studies has been the facile formation of transient aromatic-amino acid radicals (18) and the Raman saturation phenomena (19, 49a,b). The saturation phenomena derive from depopulation of the ground state and result in a power dependence of the Raman intensities. Because this power dependence strongly depends upon environment, it has been difficult to measure reliably protein aromatic amino

acid cross-sections. The recent development of lower pulse energy sources promises to surmount the present obstacles (19).

Other studies have recently examined nucleic acid bases with the objective of utilizing this information to develop techniques for monitoring DNA conformation and nucleic acid-adduct interactions (23, 90-100). Extensive RREP have been reported for adenine, thymine, uracil, cytosine, and guanine, and attempts have been made to utilize the vibrational mode intensities to determine the excited state geometry changes. These studies have been aided by the high quality normal coordinate calculations and the electronic excited state calculations that exist for these molecules (93).

Recently studies examined complexation of the antitumor agent *cis*-dichloroammine platinum (II) with GMP (95, 98) and observed specific interactions that were associated with hydrogen bonding to the carbonyl group. These preliminary results illustrate that important intermolecular interactions can be monitored. It is clear that excitation wavelengths can be chosen to enhance specifically the Raman bands of particular classes of nucleic acid bases. The DNA nucleic acid Raman cross-sections depend upon DNA coiling and base stacking due to the exciton interactions between base pairs that cause hypochromism; the Raman cross-sections often will decrease with the square of the relative absorption decrease. However, hypochromism in the resonant band does not affect all bands identically, since some bands may derive their enhancement from adjacent electronic transitions that are not hypochromic (92).

The existing aromatic amino acid and nucleic acid studies are just now being applied to examine protein and DNA conformation in *in vivo* systems (101-103). Nelson et al have recently used the relative intensities of the visible-wavelength excited carotene bands (102) and the UV excited aromatic amino acid and nucleic acid bands (103) to speciate between different algae and bacteria. Obviously, these studies represent the most aggressive applications of UV resonance Raman spectroscopy and are at the forefront of bioanalytical chemistry.

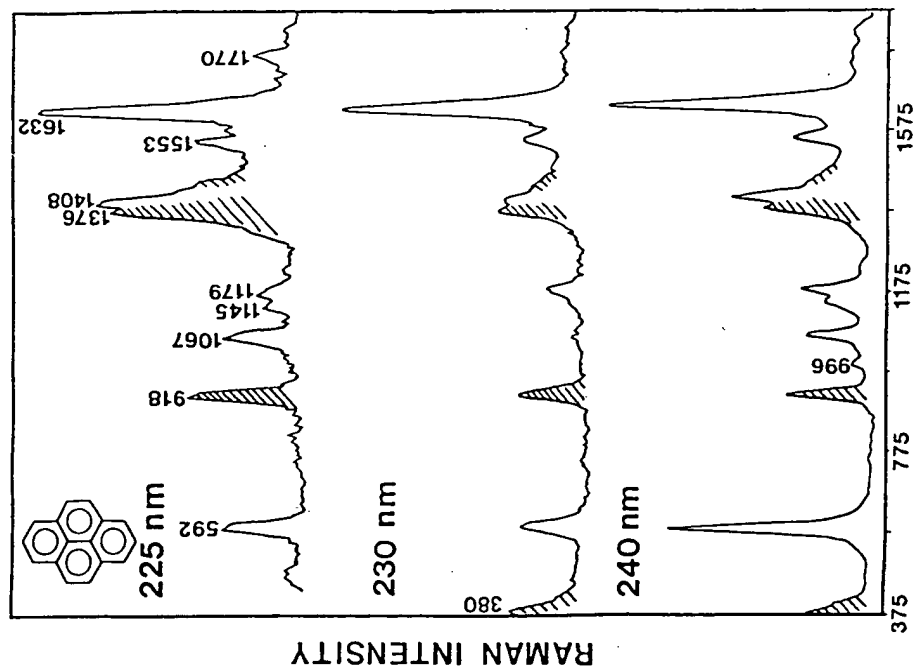
UVRR studies have been reported for more extensively conjugated molecules such as naphthalene, triphenylene, and pyrene (19, 45, 104-115). These polycyclic aromatic hydrocarbons (PAH) represent a class of molecules of significant analytical and bioanalytical interest. Other members of this class are highly carcinogenic, and all are ubiquitous in the environment. In addition, these molecules are important for electronic structure theory because they represent test cases for new theoretical calculational techniques. These large planar aromatics have strong, allowed transitions that result in huge Raman enhancements for their symmetric in-plane ring modes. For example, pyrene shows a total differential Raman cross-section of 60 Barns/stir for the 592  $\text{cm}^{-1}$  pyrene ring mode with

excitation at the maximum of its  $S_4$  transition (240 nm) (19, 45). Recent studies of the  $S_1$  (111-114) and  $S_4$  (115) transitions of azulene and the  $S_4$  transition of pyrene (45) have attempted to calculate the RREP by using the Raman transform theory. The transform formalism utilizes the Franck-Condon information available in the absorption spectrum to predict the RREP of symmetric vibrations. Excellent agreement was found for the  $S_1$  state of azulene within the framework of the transform formalism that assumes the Condon approximation. The transform theory, however, failed to model accurately the RREP of the  $S_4$  excited state of azulene, even when the theory was extended to include excited state vibrational frequency shifts or non-Condon sources of scattering (115).

In contrast, we find excellent modeling of the RREP of the  $S_4$  transition of pyrene by using the transform formalism, which includes non-Condon sources of scattering (45). Figure 19 shows the UV Raman spectra of pyrene excited in the  $S_4$  transition, while Figure 20 shows the measured absorption spectrum and RREP for the most enhanced bands. The *solid line* is the best fit of the transform calculation to the experimental RREP within the Condon approximation, while the *dashed curve* derives from a calculation that includes a small linear non-Condon contribution. Obviously, acceptable modeling of the excitation profile requires inclusion of non-Condon activity. The extent of non-Condon contributions appears to increase with the vibrational frequency from a minimum of 3% for the 1592  $\text{cm}^{-1}$  band to a maximum of 13% for the 1632  $\text{cm}^{-1}$  band. This systematic increase of the non-Condon contribution as the vibrational mode frequency increases can be diagnostic for nonadiabatic coupling between the  $S_4$  and  $S_2$  pyrene transitions.

These RREP studies examine the fundamental interactions between vibrational and electronic motion. Since much of our understanding of electronic spectroscopy derives from the numerous applications of molecular orbital calculations to rationalize the spectroscopic properties of PAHs, these studies continue to refine our understanding of excited state molecular structure and dynamics. Obviously, different transitions in PAHs exhibit different dynamical phenomena. It is striking that the RREP of the  $S_4$  transitions of pyrene and azulene can be so different, since they both appear to involve isolated, fully allowed electronic transitions that show clear Franck-Condon vibrational substructure. Future studies are expected to clarify the major differences and the importance of non-

Condon processes to electronic transitions. Other, more applied studies have utilized the UVRR selectivity and sensitivity to empirically examine PAHs such as naphthalene, triphenylene, and pyrene in samples such as coal-derived liquids, coal-liquid distillates, and rat liver microsomes (104–108). These studies illustrate the analytical



**WAVENUMBERS /cm<sup>-1</sup>**

*Figure 19* UV resonance Raman spectra of pyrene excited in the  $S_1$  electronic transition. See  $S_1$  absorption spectrum in Figure 20. The sample consists of a  $5 \times 10^{-4}$  M pyrene solution in acetonitrile. Note that the pyrene bands in the spectra show some Raman saturation. The cross-hatched bands are from the solvent. From Ref. (45).

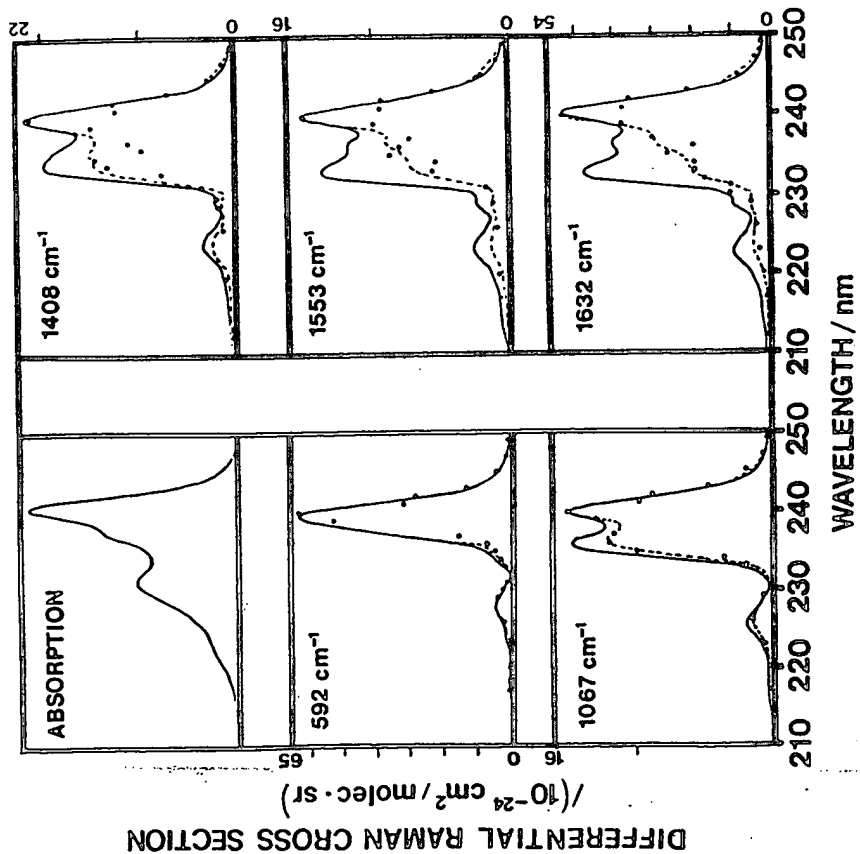


Figure 20. Absorption spectrum and RREP of symmetric vibrations of pyrene enhanced in the  $S_1$  electronic transition. The solid lines show the transform best fit if only Condon sources of scattering are assumed. The dashed lines show a transform calculation that includes non-Condon sources of scattering.

UVRR spectroscopy are now just beginning and are expected to have impact in the fuel sciences, environmental studies, and bioanalytical studies of PAH metabolism.

#### SATURATION RAMAN SPECTROSCOPY

All of the studies described above monitor Raman bands deriving from vibrational transitions in the ground state manifold. The net Raman intensity is proportional to the incident intensity, the number of molecules in the sample volume, and the Raman cross-section for the band under study.

The high peak energy fluxes of the pulsed UV excitation source can induce photophysical processes that deplete the ground state population, leading to Raman intensities that do not increase linearly with incident photon flux (18, 19, 45, 49). In addition, either permanent photoproducts or transient intermediates can form, which may also be resonant with the incident excitation frequency (18, 19, 45).

For example, Figure 21 shows the UV Raman spectra of tyrosinate excited at 488 and 245 nm. Spectra obtained at 245 nm (*B*) excited at low pulse energy fluxes show bands that are also evident in the preresonance 488 nm spectrum (*A*). In contrast, the 245 nm spectrum (*C*) excited with higher pulse energies (corresponding to ca 100 photons · mol<sup>-1</sup> · pulse<sup>-1</sup>) shows new bands that are more evident in the difference spectrum (*D*) and are easily assigned to tyrosyl radical, which transiently forms during excitation due to monophotonic ionization of tyrosine. The power dependence of the intensity of the tyrosyl radical bands indicates the quantum yield for radical formation. Further, the power dependence of the tyrosinate ground state Raman bands is quantitatively related to the ground state recovery rate. High incident energy fluxes result in an apparent saturation of the ground state Raman band intensities due to ground state depopulation.

We recently described the kinetics associated with these processes and included terms related to the quantum yield of radical formation and kinetic parameters that are used to model ground state recovery rates (18, 19, 25). In the case that negligible recovery occurs during the excitation pulse, the expressions are particularly simple.

Raman saturation can also derive from depopulation of the ground state due to population of long-lived excited states. Indeed this is the mechanism of Raman saturation in pyrene (19, 45) and tryptophan (84) associated with excitation into their upper singlet states. Efficient fast internal conversion results in population of the long-lived  $S_1$  state, which bottlenecks relaxation back to the ground state. Obviously the degree of saturation will depend upon intermolecular dynamical quenching processes that determine the lifetime of  $S_1$ .

The environmental dependence of the ground state recovery rate is the basis of a new spectroscopy we call Saturation Raman Spectroscopy that monitors relaxation back to the ground state. If relaxation is fast compared to the laser pulse length, a steady state can be built up during the excitation pulse. The steady state depopulation is directly related to the incident energy flux, the absorption cross-section (which measures the probability of transfer into the excited state), and the rate of relaxation back to the ground state. The spectroscopy monitors the dependence of the Raman intensities of ground state analyte bands upon the incident pulse energy flux.

Figures 22 and 23 illustrate one application of this spectroscopy to the study of the electronic structure of a dimer of tyrosine and tryptophan. Figure 22 shows Raman spectra of a mixture of monomeric tyrosine and tryptophan (*A* and *B*) and the Raman spectra of trp-tyr dimer (*C* and *D*) excited at 225 nm at high (*A* and *C*) and low (*B* and *D*) pulse energies. Figure 23 shows the intensity dependence of the tyrosine and tryptophan bands as a function of the incident pulse energy flux. The decreased relative tryptophan intensities (the 760  $\text{cm}^{-1}$ , 1010  $\text{cm}^{-1}$ , 1355  $\text{cm}^{-1}$ , and 1550  $\text{cm}^{-1}$  bands) in the dimer results from a hypochromic shift of the tryptophan absorption band due to the exciplex interactions. The degree of saturation differs between the Tyr and Trp residues in the monomers because of the different absorbances and relaxation rates of these residues. The hypochromic absorption decreases in the dimer are clearly evident.

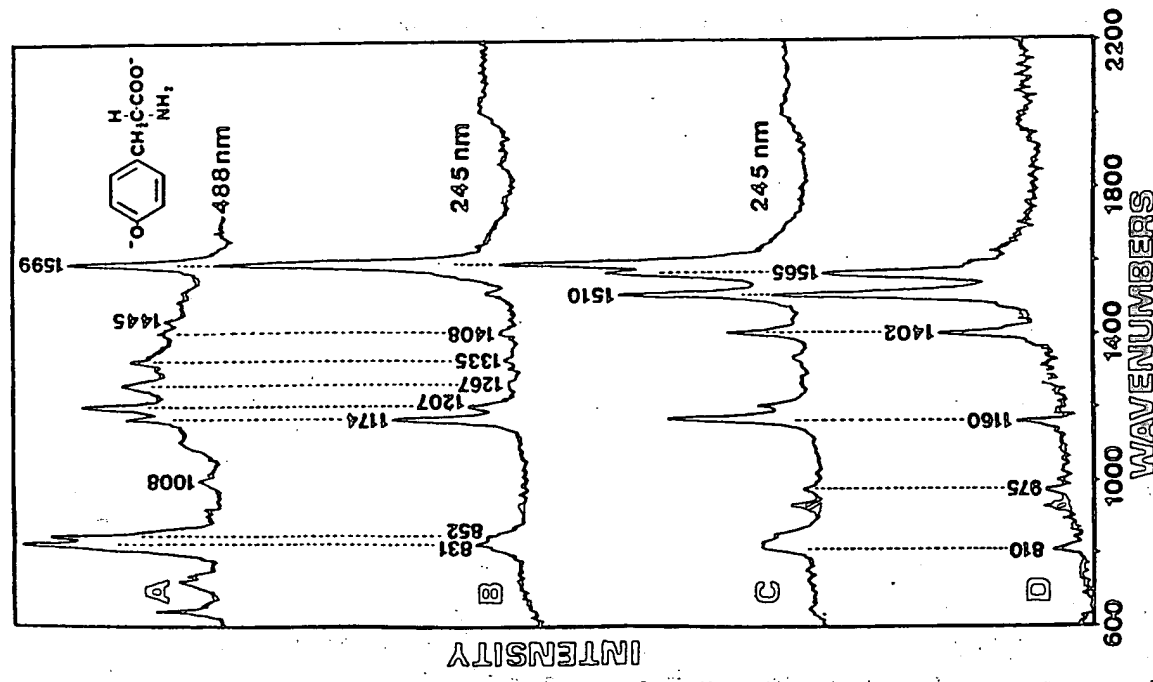


Figure 21. Raman spectra of tyrosinate in water containing 0.2 M  $\text{ClO}_4^-$  as an internal intensity standard (the shaded 932  $\text{cm}^{-1}$  band). (A) Normal Raman spectrum excited at 488 nm with a CW laser. (B) UV Raman spectrum (245 nm) excited at low pulse energy. (C) Same as *B* but at higher pulse energy. (D) Difference spectrum. *C-B*. From Ref. (18).

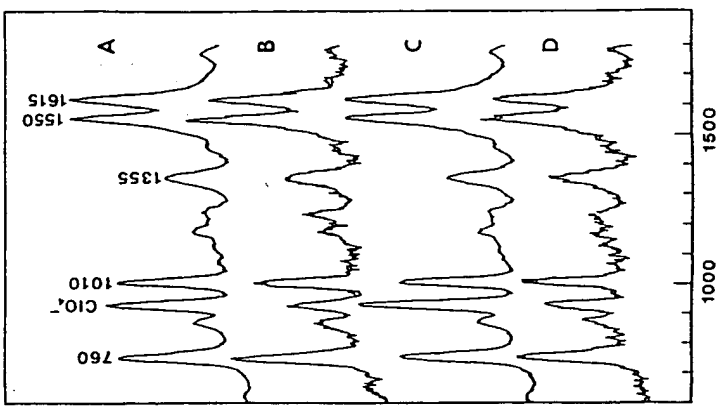


Figure 22. The pulse energy flux intensity dependence of the UV resonance Raman spectra of a stoichiometric mixture of tyrosine and tryptophan monomers, and that of the Trp-Tyr dimer excited at 225 nm. Note the 932  $\text{cm}^{-1}$   $\text{ClO}_4^-$  internal intensity standard band. From Ref. (25).

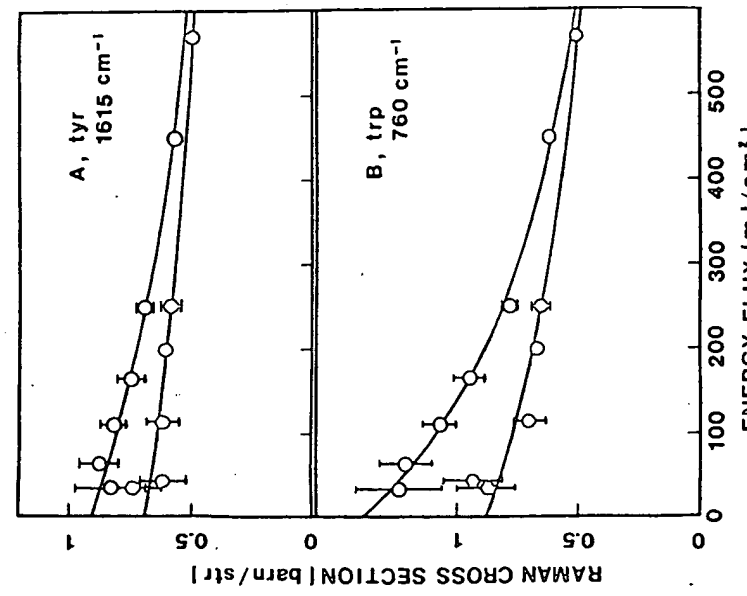


Figure 23 Dependence of Raman intensities of tyr and trp residues upon excitation pulse energy. Monomer saturation (O), dimer saturation (○). From Ref. (25).

by comparing the dimer and monomer absorption spectra. The dimer electronic transition occurs to an excited state that is a linear combination of the excited states of the tryptophan and tyrosine groups. This is evident from the saturation plot, which shows similar saturation behaviors for the tyrosine ( $1615 \text{ cm}^{-1}$ ) and the tryptophan bands in the dimer. This is also evident in the Raman spectra, since the tyr and trp relative intensities become independent of excitation power flux and the magnitude of saturation. The relaxation rate depends upon the intermolecular electronic interactions between these aromatic residues.

We expect more subtle interactions also to affect relaxation rates. For example, disulfide linkages in proteins are known to quench the fluorescence of adjacent tryptophans by increasing the rate of internal conversion. This will increase the relaxation rate back to the ground state and decrease the magnitude of Raman saturation. Indeed, we have already

observed that the extent of aromatic amino saturation depends upon the protein studied. From these preliminary studies we are hopeful that Raman Saturation Spectroscopy will prove useful in studying the environments of aromatic molecules in complex environments. Indeed, it may be possible to simplify the spectra of proteins, for example, by using pump beams to saturate particular resonances in order to study others selectively.

## HYPER-RAMAN SPECTROSCOPY

Recent studies of Ziegler et al (50-52) have demonstrated the potential utility of Resonance Hyper-Raman Spectroscopy to probe far UV excited states of molecules. Figure 24 shows that excitation at  $\nu_0$  is two-photon resonant with a far UV transition and that a photon is inelastically scattered at frequency  $2\nu_0 - \nu_v$ . For centrosymmetric molecules, resonance Raman and hyper-Raman vibrational transitions are mutually exclusive. In contrast, non-centrosymmetric molecules are expected to show hyper-Raman enhancement for the same symmetric modes as those enhanced in normal resonance Raman spectra excited at twice the frequency.

Hyper-Raman scattering appears at the  $\chi^{(3)}$  level of the electrical susceptibility. Chung & Ziegler (52) have recently reviewed the theory for spontaneous hyper-Raman scattering and have expanded it in terms of the vibronic formalism typically used in discussions of normal resonance Raman scattering. They find similar enhancement mechanisms for hyper-Raman as for normal Raman scattering. The somewhat more complex expressions can be subdivided into *A*, *B*, and *C*-term-like contributions analogous to those displayed in Eq. 8 but that uniquely display the essence of the three-photon interaction. The *A*-term enhances symmetric vibrations in electronic transitions that are both one and two-photon allowed. The *B*-term involves a vibronic transition moment and can enhance both symmetric and nonsymmetric vibrations within electronic transitions that are either/both one- or two-photon allowed. The *C*-term

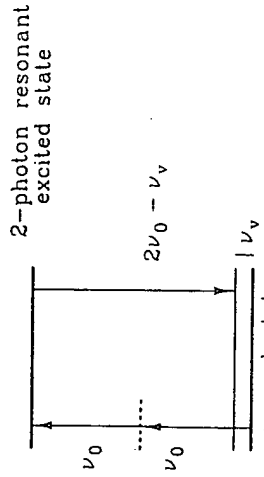


Figure 24 Energy level diagram showing hyper-Raman transition.

involves two vibronic transition moments and can be involved in Franck-Condon scattering of symmetric vibrations and overtones and combinations of nonsymmetric modes. The C-term is expected to be a weak source of resonance hyper-Raman enhancement.

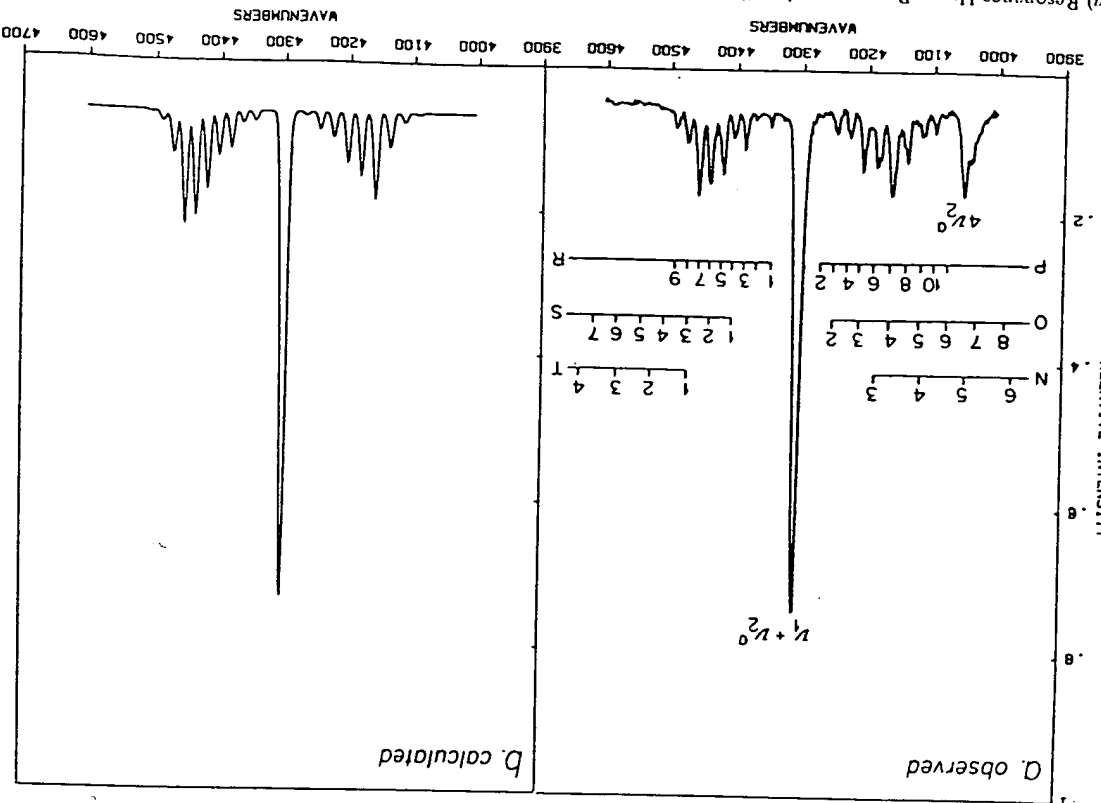
Figure 25 shows the resonance hyper-Raman spectrum of ammonia excited at 425.6 nm and the calculated spectrum used to determine the excited state lifetime. Obviously the signal-to-noise ratios are comparable to those obtained by direct resonance Raman measurements of ammonia in the UV (see Figures 7 and 8), in spite of the dramatically decreased hyper-Raman cross-sections. This occurs because self-absorption of the incident excitation beam does not occur for the visible wavelength excitation; higher sample concentrations can be used and the beam can sample larger volume elements. A major advantage for hyper-Raman studies of far UV transitions is that the hyper-Raman excitation utilizes tunable visible wavelength excitation sources that have high power fluxes. In addition, little competing absorption and photochemistry occurs with visible excitation, in contrast to far UV excitation. Although not proven, it is possible that less stray-light spectral interferences may occur for hyper-Raman, since the cross-sections for the hyper-Rayleigh elastic scattering from particulates and refractive index inhomogeneities may be smaller relative to the vibrational hyper-Raman cross-sections than for normal Raman scattering.

It is likely that hyper-resonance Raman spectroscopy will prove to be an important new technique for studying far UV-excited states. Studies of ammonia,  $\text{CH}_3\text{J}$ , and  $\text{CS}_2$  illustrate the A- and B-term like resonance hyper-Raman enhancement mechanisms (52). Future studies are likely to prove the utility of this technique for studying condensed phase systems as well.

## CONCLUSIONS

This review was written in the winter of 1987, a period of active progress in fundamental and applied UV Raman studies. It is already clear that new information is being obtained that both confirms and leads the theoretical understanding of electronic structure and dynamics. The future directions of research will probe electronic-vibrational rotational coupling in small molecules as well as use this spectroscopy in applications in physical chemistry, physical organic, biophysical chemistry, analytical chemistry, and bioanalytical chemistry. At the moment the experimental limitations derive mainly from the inconvenience of the present high pulse energy flux UV excitations sources. These limitations are rapidly disappearing as new technology develops.

(b) Calculated spectrum, which gives an excited state lifetime of 130 fscc. From Rec. (50).



ACKNOWLEDGMENTS

gratefully acknowledge the work of the present and past members of my research group who made the progress reviewed here. Special thanks go to Dr. Colleen Jones, Val DeVito, Paul Harmon, and Dr. Junji Teraoka or their results that were filched prior to publication and for their helpful comments. I also gratefully acknowledge preprints and helpful conversations with Dr. Larry Ziegler, Dr. Bruce Hudson, and Dr. Tom Spiro. I also gratefully acknowledge support for this work from National Institute of Health Grant 1R01 GM30741-07. Sanford A. Asher is an Established Investigator of the American Heart Association; this work was done during one tenure of an Established Investigatorship of the American Heart Association, Pennsylvania affiliate.

### Literature Cited

- macker, K. T., Champion, P. M. 1984. *J. Am. Chem. Soc.* 106: 5698.
84. Asher, S. A., Ludwig, M., Johnson, C. R. 1986. *J. Am. Chem. Soc.* 108: 3186.
85. Rava, R. P., Spiro, T. G. 1984. *J. Am. Chem. Soc.* 106: 4062.
86. Rava, R. P., Spiro, T. G. 1985. *J. Phys. Chem.* 89: 1856.
87. Cawell, D. S., Spiro, T. G. 1986. *J. Am. Chem. Soc.* 108: 6470.
88. Cawell, D. S., Spiro, T. G. 1986. *Biochim. Biophys. Acta* 873: 73.
89. Hildebrand, P. G., Copeland, R. A., Spiro, T. G., Olewski, J., Laskowski, M., Prendergast, F. G. 1988. *Biochemistry, Submitted*.
90. Fodor, S. P. A., Rava, R., Hays, T. R., Spiro, T. G. 1985. *J. Am. Chem. Soc.* 107: 1320.
91. Copeland, R. A., Spiro, T. G. 1986. *J. Phys. Chem.* 90: 6648.
92. Fodor, S. P. A., Spiro, T. G. 1986. *J. Am. Chem. Soc.* 108: 3198.
93. Tsuji, M., Nishimura, Y., Hirakawa, A. Y., Petricolas, W. L. 1987. In *Biological Applications of Raman Spectroscopy*, Vol. 2, ed. T. G. Spiro. New York: Wiley.
94. Wang, Y., Petricolas, W. L. 1987. *J. Phys. Chem.* 91: 3122.
95. Ziegler, L. D., Hudson, B., Strommen, D. P., Petricolas, W. L. 1984. *Bio-polymers* 23: 2067.
96. Kubasek, W. L., Hudson, B., Petricolas, W. L. 1985. *Proc. Natl. Acad. Sci. USA* 82: 2369.
97. Blaize, D. C., Petricolas, W. L. 1980. *J. Chem. Phys.* 72: 3134.
98. Perio, J. R., Cwikel, D., Spiro, T. G. 1987. *Inorg. Chem.* 26: 400.
99. Chinsky, L., Turpin, P. Y., Duquesne, M., Brahms, J. 1977. *Biochem. Biophys. Res. Commun.* 75: 766.
100. Chinsky, L., Turpin, P. Y., Duquesne, M., Brahms, J. 1978. *Biopolymers* 17: 1347.
101. Nocentini, S., Chinsky, L. 1983. *J. Raman Spectrosc.* 14: 9.
102. Dalterio, R. A., Baek, M., Nelson, W. H., Britt, D., Sperry, J. F., Purcell, F. J. 1987. *Appl. Spectrosc.* 41: 241.
103. Dalterio, R. A., Nelson, W. H., Britt, D., Sperry, J. F. 1987. *Appl. Spectrosc.* 41: 417.
104. Asher, S. A. 1984. *Anal. Chem.* 56: 720.
105. Asher, S. A., Johnson, C. R. 1984. *Science* 225: 311.
106. Johnson, C. R., Asher, S. A. 1984. *Anal. Chem.* 56: 2258.
- 107a. Jones, C. M., Naim, T. A., Ludwig, M., Murlough, J., Flaugher, P. I., Dudik, T. M., Johnson, C. R., Asher, S. A. 1985. *Trac-Trends Anal. Chem.* 4: 75.
- 107b. Asher, S. A., Jones, C. M. 1986. In *New Applications of Analytical Techniques to Fossil Fuels*, ed. M. Perry, H. Retcofsky, ACS Div. Fuel Chem. Preprints 31: 170.
108. Rumelfanger, R., Asher, S. A., Perry, M. B. 1988. *Appl. Spectrosc.* 42: 267.
109. Petricolas, W. L., Chinsky, L., Turpin, P. Y., Laigle, A. 1983. *J. Chem. Phys.* 78: 656.
110. Koshihara, S., Kobayashi, T. 1986. *J. Chem. Phys.* 85: 1211.
111. Liang, R., Schnapp, O., Warshel, A. 1976. *Chem. Phys. Lett.* 44: 394.
112. Liang, R., Schnapp, O., Warshel, A. 1978. *Chem. Phys.* 34: 17.
113. Braffman, O., Chan, C. K., Khodadoost, B., Page, J. B., Walker, C. T. 1984. *J. Chem. Phys.* 80: 5406.
114. Chan, C. K., Page, J. B., Tonks, D. L., Braffman, O., Khodadoost, B., Walker, C. T. 1985. *J. Chem. Phys.* 82: 4813.
115. Cable, J. R., Albrecht, A. C. 1986. *J. Chem. Phys.* 84: 1969.

## INTRODUCTION

This review is primarily concerned with the identification of the structures of chemisorbed complexes formed between hydrocarbons and metal surfaces through the use of various forms of vibrational spectroscopy (1). The identification of the chemisorbed species and the study of their reactivities by spectroscopic methods provides an essential basis for the understanding of many classes of metal-catalyzed reactions of hydrocarbons such as hydrogenation/dehydrogenation, hydrogenolysis, isomerization, and metathesis.

The particular emphasis of this article is on the study of species formed on metal single crystals that are cut so that specific surfaces of known atomic arrangements, e.g. the [111], [100], and [110] surfaces of face-centered cubic (fcc) metals, are exposed to the hydrocarbon adsorbate. Such experiments have become feasible during the past 15 years or so. The principal vibrational spectroscopic techniques used for this purpose are high resolution electron energy loss spectroscopy (EELS) (2) and reflection/absorption infrared spectroscopy (RAIRS) (3).

In recent years it has been shown that results obtained with these simplified single-crystal systems are of great value in interpreting